

Exploring the Plasma Chemistry in Microwave Chemical Vapor Deposition of Diamond from C/H/O Gas Mixtures

Mark W. Kelly, James C. Richley, Colin M. Western, and Michael N. R. Ashfold*

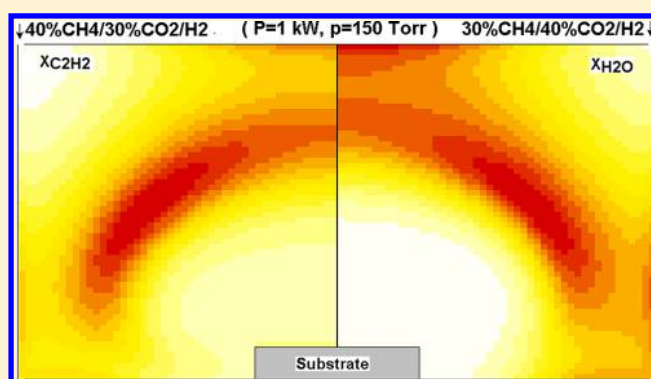
School of Chemistry, University of Bristol, Bristol BS8 1TS, U.K.

Yuri A. Mankelevich

Skobel'tsyn Institute of Nuclear Physics, Moscow State University, Leninskie Gory, Moscow 119991, Russia

Supporting Information

ABSTRACT: Microwave (MW)-activated CH₄/CO₂/H₂ gas mixtures operating under conditions relevant to diamond chemical vapor deposition (i.e., $X_{C/\Sigma} = X_{\text{elem}}(\text{C}) / (X_{\text{elem}}(\text{C}) + X_{\text{elem}}(\text{O})) \approx 0.5$, H₂ mole fraction = 0.3, pressure, $p = 150$ Torr, and input power, $P = 1$ kW) have been explored in detail by a combination of spatially resolved absorption measurements (of CH, C₂(a), and OH radicals and H($n = 2$) atoms) within the hot plasma region and companion 2-dimensional modeling of the plasma. CO and H₂ are identified as the dominant species in the plasma core. The lower thermal conductivity of such a mixture (cf. the H₂-rich plasmas used in most diamond chemical vapor deposition) accounts for the finding that CH₄/CO₂/H₂ plasmas can yield similar maximal gas temperatures and diamond growth rates at lower input powers than traditional CH₄/H₂ plasmas. The plasma chemistry and composition is seen to switch upon changing from oxygen-rich ($X_{C/\Sigma} < 0.5$) to carbon-rich ($X_{C/\Sigma} > 0.5$) source gas mixtures and, by comparing CH₄/CO₂/H₂ ($X_{C/\Sigma} = 0.5$) and CO/H₂ plasmas, to be sensitive to the choice of source gas (by virtue of the different prevailing gas activation mechanisms), in contrast to C/H process gas mixtures. CH₃ radicals are identified as the most abundant C₁H_{*x*} [$x = 0-3$] species near the growing diamond surface within the process window for successful diamond growth ($X_{C/\Sigma} \approx 0.5-0.54$) identified by Bachmann et al. (*Diamond Relat. Mater.* **1991**, *1*, 1). This, and the findings of similar maximal gas temperatures ($T_{\text{gas}} \sim 2800-3000$ K) and H atom mole fractions ($X(\text{H}) \sim 5-10\%$) to those found in MW-activated C/H plasmas, points to the prevalence of similar CH₃ radical based diamond growth mechanisms in both C/H and C/H/O plasmas.



1. INTRODUCTION

The Bachmann diagram¹ provides a very convenient overview of the C/H/O gas mixing ratios required for successful diamond chemical vapor deposition (CVD). Most CVD diamonds are currently grown from C/H (typically CH₄/H₂) gas mixtures,^{2,3} but early studies explored a range of C/H/O source gas mixtures, from the perspectives of the gas phase chemistry and composition (as deduced by optical emission spectroscopy (OES) and/or mass spectrometry) and of the growth rate and quality of the resulting diamond.⁴⁻¹¹ These early studies demonstrated that successful diamond growth was restricted to compositions very close to the H-CO tie line in Figure 1 and suggested that C/H/O plasmas offered a route to growing diamond at lower substrate temperatures (T_{sub}) than with the traditional C/H gas mixtures. Mollart and Lewis¹² reported a comprehensive study of microwave (MW) activated CH₄/CO₂ and C₂H₄/CO₂ mixtures (with and without additional H₂), which demonstrated formation of high quality polycrystalline diamond films at commercially viable growth rates. The highest quality material, as judged by the width of

the 1332 cm⁻¹ diamond feature in the Raman spectrum, was achieved using a stoichiometric CH₄/CO₂ mixture (i.e., one that sits on the H-CO tie line) with additional H₂. Even a small excess of CH₄ over CO₂ resulted in noticeably poorer quality material. Vandenbulcke and co-workers^{13,14} have reported diagnostic and modeling studies of low pressure MW-activated C/H/O gas mixtures and of the polycrystalline diamond derived there from. For completeness, we note that the possible benefits of adding trace quantities of oxygen to C/H process gas mixtures (as O₂ or as another O containing species like CO or CO₂) in order to reduce nitrogen incorporation and cracking in CVD grown single crystal diamond,^{15,16} and as a means of inhibiting [110] growth in heavily B-doped diamond¹⁷ have also been explored.

Given recent successes in the quantitative diagnosis and modeling of MW-activated C/H/Ar gas mixtures (with and

Received: June 23, 2012

Revised: August 15, 2012

Published: August 27, 2012



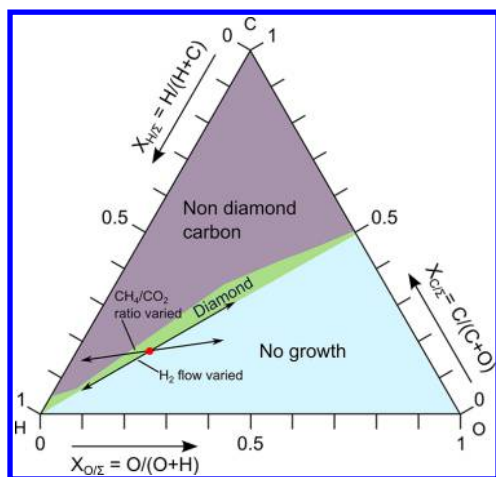


Figure 1. C–H–O Bachmann diagram, illustrating the H–CO tie line and the composition regions probed by varying the flow rate $F(\text{H}_2)$ and the ratio $X_{\text{C}/\Sigma}$ when $X_0(\text{H}_2) = 0.3$ (marked with a red spot).

without trace B additions),^{18–23} the time is now ripe for a rigorous investigation of C/H/O plasmas with a view to testing their utility for commercial diamond CVD. As in our other recent studies, we combine spatially resolved gas phase spectroscopy with 2-dimensional (2-D) modeling of the essential processes occurring in a MW plasma enhanced (PE) CVD reactor to gain a detailed and systematic understanding of the chemistry and composition of C/H/O (i.e., $\text{CH}_4/\text{CO}_2/\text{H}_2$ and CO/H_2) based plasmas and their variation with process conditions. The available experimental methods include cavity ring down spectroscopy (CRDS) and optical emission spectroscopy (OES). The former is a highly sensitive, laser based absorption technique that can yield absolute column densities of transient species localized within the hot plasma region (e.g., CH , $\text{C}_2(a)$ and OH radicals, and $\text{H}(n=2)$ atoms), which serve to benchmark key elements of the 2-D modeling. The results presented here and in the companion article:²⁴

- (i) Provide the first detailed diagnosis and interpretation of the gas processing within MW-activated C/H/O mixtures under conditions relevant to diamond CVD.
- (ii) Show that, in contrast to C/H gas mixtures, the plasma composition can be sensitively dependent upon the chosen C/H/O source gas mixture (e.g., the plasma-chemical gas activation mechanisms of elementally equivalent $\text{CH}_4/\text{CO}_2/\text{H}_2$ and CO/H_2 mixtures are shown to be markedly different).
- (iii) Highlight the obvious switch in plasma chemistry that occurs on passing through the H–CO tie line (i.e. from an oxygen-rich to a carbon-rich plasma), thereby providing a rationale for the previously recognized sensitivity of the diamond process window to input gas mixing ratio (as shown by the Bachmann diagram).
- (iv) Identify CH_3 radicals as the most abundant of the C_1H_x [$x = 0–3$] hydrocarbon radical species near the growing diamond surface, suggesting that (as with C/H gas mixtures) CH_3 is likely to be the main species responsible for diamond growth.
- (v) Sound a note of caution regarding the interpretation of OES data²⁴ when, as here, exothermic reactions within the hot plasma region yield chemiluminescent products that supplement the emission generated by electron impact excitation.

This article focuses on spatially resolved CRDS measurements of the chosen target species, as functions of process conditions, and 2-D modeling of the gas phase chemistry that provides the first quantitative description of the chemistry and composition prevailing in C/H/O plasmas operating at input powers and pressures relevant to commercial diamond CVD.

2. EXPERIMENTAL SECTION

The MW PECVD reactor, the laser system, and the optical arrangements for the spatially resolved CRDS (and OES) measurements as functions of height (z) above the substrate on which diamond growth occurs have all been described previously.^{19,20} A new feature of the present study is the measurement of $\text{OH}(X, \nu = 0)$ radicals by CRDS. This typically focuses on the three unblended lines shown in Figure 2, selected on the basis that they span a sufficient range of

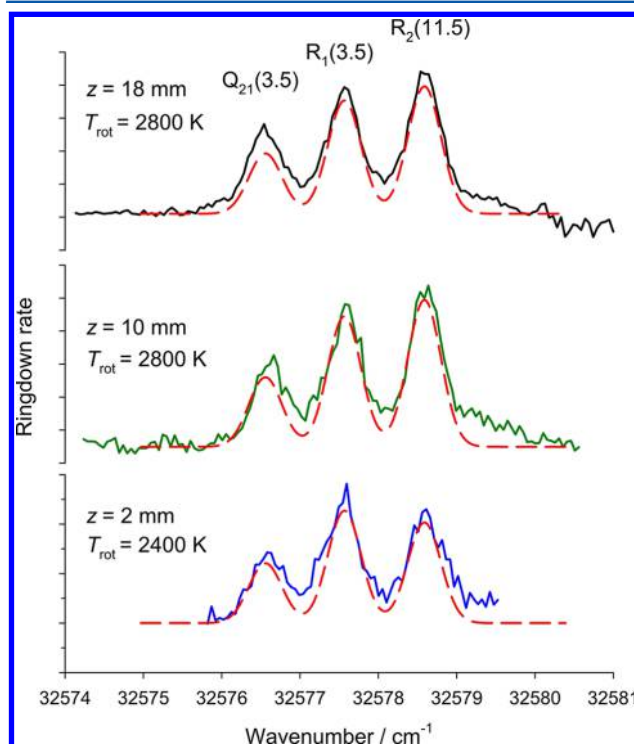


Figure 2. Part of the $\text{OH}(A^2\Sigma^+ - X^2\Pi)$ (0,0) band measured by CRDS in a $\text{CH}_4/\text{CO}_2/\text{H}_2$ plasma at $z = 18, 10,$ and 2 mm (top, middle, and bottom) for base conditions ($X_{\text{C}/\Sigma} = 0.5$, $X_0(\text{H}_2) = 0.3$, $p = 150$ Torr, $P = 1$ kW) showing the individual line assignments, along with PGOPHER simulations (dashed lines) of the relevant part of the overall band contour assuming $T_{\text{rot}} = 2800$ K (top and middle) and 2400 K (bottom).

internal energies to allow reliable estimation of the rotational temperature (T_{rot}) and hence absolute column densities.

The CH_4 , CO_2 , H_2 , and CO process gases were metered through separate, calibrated mass flow controllers (MFCs) and premixed prior to entering the reactor through two diametrically opposed $1/4$ " stainless steel pipes located close beneath the quartz window that defines the top of the reactor and at an angle of $\sim 45^\circ$ to the probe axis. Base conditions for the $\text{CH}_4/\text{CO}_2/\text{H}_2$ plasma were chosen to be total pressure, $p = 150$ Torr, input power, $P = 1$ kW, and input flow rates, $F(\text{CH}_4) = F(\text{CO}_2) = 175$ standard cm^3 per minute (sccm), $F(\text{H}_2) = 150$ sccm. For compactness, we use the $X_{\text{C}/\Sigma}$ notation¹ to describe the various gas mixtures and define $X_{\text{C}/\Sigma}$ as $X_{\text{elem}}(\text{C})/[X_{\text{elem}}(\text{C}) +$

Table 1. Radiative and Temperature Dependent Line Strengths (p_{line} Factors, from PGOPHER²⁵) for the Probe Transitions Used to Monitor $\text{C}_2(\text{a}, \nu = 0)$, $\text{CH}(\text{X}, \nu = 0)$, and $\text{OH}(\text{X}, \nu = 0)$ Radical Column Densities

transition	$\text{C}_2(\text{d-a}) (0,0)$	$\text{CH}(\text{A-X}) (0,0)$	$\text{OH}(\text{A-X}) (0,0)$	
$A (s^{-1})$	$(7.21 \pm 0.30) \times 10^{6a}$	$(1.85 \pm 0.05) \times 10^{6a}$	1.315×10^{6b}	
g_u	6	4	2	
g_l	6	4	4	
$T (K)$	p_{line} factors from PGOPHER			
	$\text{C}_2(\text{d-a}) 0,0$			
	$R_{3f}(8)$	$R_{2e}(9)$	$R_{1f}(10)$	$P_{3e}(37)$
3200	0.00230	0.00253	0.00279	0.00350
3000	0.00244	0.00269	0.00296	0.00347
2800	0.00261	0.00287	0.00317	0.00343
2600	0.00280	0.00308	0.00339	0.00336
	$\text{CH}(\text{A-X}) 0,0$			
	$R_{1e}(15)$	$R_{1f}(15) + R_{2f}(13)$	$R_{2e}(13)$	
3200	0.00466	0.00882	0.00416	
3000	0.00487	0.00921	0.00432	
2800	0.00509	0.00963	0.00454	
2600	0.00532	0.01000	0.00475	
	$\text{OH}(\text{A-X}) 0,0$			
	$Q_{21}(3,5)$	$R_1(3,5)$	$R_2(11,5)$	$R_2(6,5)$
3000	0.00269	0.00505	0.00622	0.00812
2800	0.00287	0.00539	0.00605	0.00841
2600	0.00307	0.00577	0.00584	0.00870
2400	0.00330	0.00621	0.00555	0.00900

^aReference 28. ^bFrom refs 29 and 30.

$X_{\text{elem}}(\text{O})$] in the source gas mixture. $X_{\text{elem}}(\text{C})$, the elemental carbon mole fraction, for example, is calculated as the elemental carbon flow rate relative to the total elemental flow rate, i.e., $X_{\text{elem}}(\text{C}) = [F(\text{CH}_4) + F(\text{CO}_2)]/[5F(\text{CH}_4) + 3F(\text{CO}_2) + 2F(\text{H}_2)]$. For a $\text{CH}_4/\text{CO}_2/\text{H}_2$ mixture, therefore, $X_{\text{C}/\Sigma} = [X_0(\text{CH}_4) + X_0(\text{CO}_2)]/[X_0(\text{CH}_4) + 3X_0(\text{CO}_2)]$, where the X_0 are the respective input mole fractions. Base conditions thus correspond to $X_{\text{C}/\Sigma} = 0.5$ and $X_0(\text{H}_2) = 0.3$. When varying one parameter, all others were maintained at their base values except when investigating the effect of altering the respective gas flow rates. Variations in $X_{\text{C}/\Sigma}$ at a given $X_0(\text{H}_2)$ were explored by adjusting $F(\text{CH}_4)$ to compensate for any change in $F(\text{CO}_2)$. The effects of varying $X_0(\text{H}_2)$ were explored by maintaining $X_{\text{C}/\Sigma}$ constant and adjusting $\{F(\text{CH}_4) + F(\text{CO}_2)\}$ so as to compensate for any change in $F(\text{H}_2)$. CO/H_2 plasmas offer a smaller parameter space since $X_{\text{C}/\Sigma}$ is necessarily 0.5. For comparison purposes, we here focus on a CO/H_2 mixture with the same C/H/O elemental ratio as the base 35% CH_4 /35% CO_2 /30% H_2 mixture (i.e., the $X_{\text{eq}}(\text{CO})/X_{\text{eq}}(\text{H}_2)$ mixture with CO mole fraction $X_{\text{eq}}(\text{CO}) = (1 - X_0(\text{H}_2))/[2 - X_0(\text{H}_2)] = 0.412$ and thus $X_{\text{eq}}(\text{H}_2) = 0.588$, with $p = 150$ Torr, $P = 1$ kW, and $F_{\text{total}} = 500$ sccm.

3. EXPERIMENTAL RESULTS

3.1. Gas Temperature Determinations. Figure 2 shows part of the $\text{OH}(\text{A-X}) (\nu' = 0, \nu'' = 0)$ band measured by CRDS along the column at $z = 2, 10,$ and 18 mm above the substrate surface under base conditions ($\text{CH}_4/\text{CO}_2/\text{H}_2$ plasma, $X_{\text{C}/\Sigma} = 0.5$, $X_0(\text{H}_2) = 0.3$, $p = 150$ Torr, $P = 1$ kW), along with the three line assignments. The spectral simulation program PGOPHER²⁵ was used to fit the line listing for the $\text{OH}(\text{A-X}) (0,0)$ band contained in the HITRAN database,²⁶ thereby yielding the best available spectroscopic constants for the $X(\nu'' = 0)$ and $A(\nu' = 0)$ states and enabling simulation of the complete band profile for a range of rotational temperatures.

The dashed profiles beneath the three experimental spectra show the best-fit simulations of the relevant spectral region and the associated T_{rot} values. These range from ~ 2400 K at $z = 2$ mm to ~ 2800 K at $z = 10$ and 18 mm. The efficiency of rotational \rightarrow translational ($R \rightarrow T$) energy transfer at the prevailing pressures encourages local thermodynamic equilibrium and validates the assumption that T_{rot} provides a measure of the local gas temperature, T_{gas} . We do recognize, however, that the values so derived are (number density weighted) average temperatures along that part of the probed column in which the $\text{OH}(\text{X})_{\nu=0}$ radicals are concentrated. The measured T_{rot} values indicate that the OH radicals are localized in and/or near the hot plasma region; the lower value at $z = 2$ mm is consistent with the proximity of the cooler substrate (the surface of which is estimated to be ~ 1070 K by optical pyrometry) and the water cooled base plate. Measurements of individual line intensities within the $\text{C}_2(\text{d-a})$ system are often used to determine T_{gas} in MW-activated C/H/Ar plasmas.^{19,23,27} As shown below, $\text{C}_2(\text{d-a})$ absorption is undetectable in C/H/O plasmas with $X_{\text{C}/\Sigma} < 0.5$ but grows rapidly once $X_{\text{C}/\Sigma} > 0.5$. Fitting $\text{C}_2(\text{d-a})$ CRDS spectra recorded from C/H/O plasmas operating with $X_{\text{C}/\Sigma} = 0.51$, $X_0(\text{H}_2) = 0.3$ and base p and P at $z = 10$ mm returns $T_{\text{rot}} = 3000 \pm 100$ K suggesting that, under these conditions and relative to $\text{OH}(\text{X})$, the $\text{C}_2(\text{a})$ radicals are more tightly localized in the hot plasma region.

3.2. Spatial Profiles. As before,¹⁹ given T_{gas} , eq 1 can be used to convert a measured change in ring down rate (Δk , in s^{-1}) versus wavenumber ($\bar{\nu}$, in cm^{-1}) associated with a given spectral line into the absolute column density $\{D\}$ of the relevant spectral carrier

$$\{D\} = \frac{8\pi L \bar{\nu}^2 g_l}{A p_{\text{line}} g_u} \int_{\text{line}} \Delta k d\bar{\nu} \quad (1)$$

L in eq 1 is the length of the ring down cavity (84 cm), A is the Einstein A coefficient for the particular vibronic transition of interest, g_u and g_l are the electronic degeneracies of the upper and lower states, and p_{line} is a transition and temperature dependent weighting factor calculated using PGOPHER.²⁵ Specifically, p_{line} is the ratio of the integrated intensity of the spectral line under study to the total band intensity (i.e., the sum of the integrated intensities of every rotational feature within the band). Table 1 lists the values adopted for A , g_u , g_l , and p_{line} (for selected lines and gas temperatures) for the molecular species probed in the present study. The A coefficients assumed for the $\text{C}_2(\text{d-a})$ and $\text{CH}(\text{A-X})$ origin transitions have been reported previously,²⁸ while that for the $\text{OH}(\text{A-X})$ (0,0) band is obtained from the fluorescence lifetime (688 ns for the A , $v' = 0$ level)²⁹ and the Franck–Condon factor, $q_{00} = 0.905$.³⁰

The procedure for obtaining $\text{H}(n = 2)$ column densities from CRDS measurements on the $n = 3 \leftarrow n = 2$ Balmer- α transition has also been described previously.^{31,32} Explicit knowledge of T_{gas} is not necessary to convert measured ring down data into column densities in this case, but Einstein A coefficients are required for all fine-structure components of the transition.³³ All spin–orbit components arising from the $2s^1$ and $2p^1$ electronic configurations are assumed to be populated statistically (in accord with their orbital degeneracies), and each of the seven fine-structure transitions is assumed to display the same full width at half-maximum (fwhm) line width. The line width of each fine-structure transition returned by least-squares fitting to the measured line shape ($\sim 0.75 \text{ cm}^{-1}$) is greater than that expected for $T_{\text{gas}} \approx 3000 \text{ K}$; as found in previous studies of MW-activated $\text{C}/\text{H}/\text{Ar}$ plasmas.¹⁹ We return to discuss this observation later.

Figure 3a shows z -dependent profiles for $\{\text{H}(n = 2)\}$, $\{\text{C}_2(\text{a}, v = 0)\}$, $\{\text{CH}(\text{X}, v = 0)\}$, and $\{\text{OH}(\text{X}, v = 0)\}$ obtained by CRDS probing of a $\text{CH}_4/\text{CO}_2/\text{H}_2$ plasma operating under base conditions with $X_{\text{C}/\Sigma} = 0.5$ (for OH) and $X_{\text{C}/\Sigma} = 0.505$ for all other species. The maximum value of $\{\text{OH}(\text{X}, v = 0)\}$ under base conditions is at least 1 order of magnitude greater than that of $\{\text{CH}(\text{X}, v = 0)\}$, which itself is about an order of magnitude larger than $\{\text{C}_2(\text{a}, v = 0)\}$. The $\text{C}_2(\text{a})$ and $\text{C}_2(\text{X})$ populations are expected to be in local thermodynamic equilibrium under the prevailing conditions,³⁴ so the 6-fold degeneracy of the $a^3\Pi$ state ensures that $\sim 75\%$ of the total C_2 radical population will be in this state. All of the measured column densities fall sharply on approaching the substrate (small z), but the data reveal a systematic shift in peak column density from $z \approx 7 \text{ mm}$ for $\text{H}(n = 2)$, $z \approx 8.5 \text{ mm}$ for $\text{C}_2(\text{a})$ and $\text{CH}(\text{X})$, and $z \approx 10 \text{ mm}$ for $\text{OH}(\text{X})$. The $\text{OH}(\text{X})$ distribution is clearly the most extensive, declining more slowly at large z than $\{\text{C}_2(\text{a}, v = 0)\}$ and $\{\text{CH}(\text{X}, v = 0)\}$, for example. This serves to reinforce the impression gained from the deduced T_{gas} values that the $\text{OH}(\text{X})$ radicals at base conditions are distributed over a larger volume than any of the other transient species probed; spatially resolved CRDS studies of $\text{OH}(\text{X})$ at $X_{\text{C}/\Sigma} = 0.49$ return a very similar spatial profile. Also included in Figure 3a are the $\text{CH}(\text{X}, v = 0)$, and $\text{OH}(\text{X}, v = 0)$, column densities measured in the base CO/H_2 plasma operating at the same p and P ; both column densities are noticeably lower than in the corresponding $\text{CH}_4/\text{CO}_2/\text{H}_2$ plasma. The corresponding quantities returned by the present 2-D modeling are shown in Figure 3b; agreements and discrepancies between measured and predicted quantities are considered in section 4.

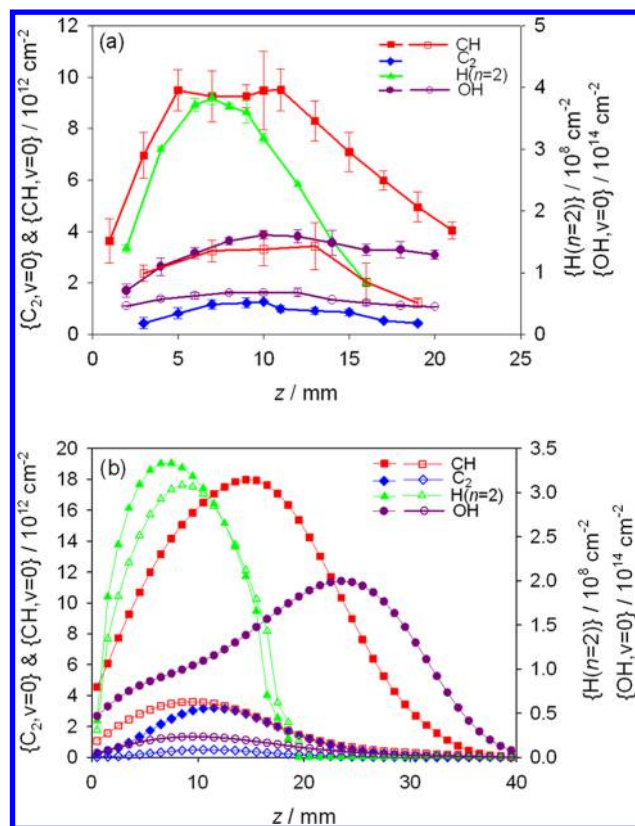


Figure 3. (a) z -dependent column densities of (solid symbols) $\text{H}(n = 2)$ atoms and $\text{C}_2(\text{a}, v = 0)$, $\text{CH}(\text{X}, v = 0)$, and $\text{OH}(\text{X}, v = 0)$ radicals measured by CRDS in a $\text{CH}_4/\text{CO}_2/\text{H}_2$ plasma operating at base conditions, with $X_{\text{C}/\Sigma} = 0.5$ (for OH) and $X_{\text{C}/\Sigma} = 0.505$ (for all other species) and (open symbols) $\{\text{CH}(\text{X}, v = 0)\}$ and $\{\text{OH}(\text{X}, v = 0)\}$ in the 41.2% $\text{CO}/58.8\%$ H_2 plasma operating at base p , P , and F_{total} . (b) z -dependent column densities returned by the 2-D model calculations for $\text{H}(n = 2)$ atoms and $\text{C}_2(\text{a}, v = 0)$, $\text{CH}(\text{X}, v = 0)$, and $\text{OH}(\text{X}, v = 0)$ radicals in a 35% $\text{CH}_4/35\%$ $\text{CO}_2/30\%$ H_2 plasma running at base conditions (solid symbols) and in a 41.2% $\text{CO}/58.8\%$ H_2 plasma operating at base p , P , and F_{total} (open symbols).

3.3. Sensitivity to CH_4/CO_2 Ratio and to $X_0(\text{H}_2)$. Figure 4 shows the way in which the column densities of each of the species in a $\text{CH}_4/\text{CO}_2/\text{H}_2$ plasma probed at $z = 10 \text{ mm}$ (i.e., near the maximum of the column densities of the radical species but above the center of the $\text{H}(n = 2)$ distribution) vary with $X_{\text{C}/\Sigma}$ when $X_0(\text{H}_2) =$ (a) 0.3 and (b) 0.6. Increasing $X_{\text{C}/\Sigma}$ from 0.49 to 0.51 at $X_0(\text{H}_2) = 0.3$ (Figure 4a) leads to an order of magnitude drop in $\{\text{OH}(\text{X}, v = 0)\}$ and a 5-fold increase in $\{\text{CH}(\text{X}, v = 0)\}$; the column densities of both of these species are relatively constant on either side of this region. $\{\text{C}_2(\text{a}, v = 0)\}$ is undetectable at $X_{\text{C}/\Sigma} = 0.49$ but increases steeply once $X_{\text{C}/\Sigma} \geq 0.5$. $\{\text{H}(n = 2)\}$ increases $\sim 50\%$ upon raising $X_{\text{C}/\Sigma}$ from 0.49 to 0.51. These trends are all also evident in the data recorded with $X_0(\text{H}_2) = 0.6$ (Figure 4b), but the step-change around $X_{\text{C}/\Sigma} \approx 0.5$ is more gradual. $\{\text{H}(n = 2)\}$ and $\{\text{OH}(\text{X}, v = 0)\}$ at $X_{\text{C}/\Sigma} < 0.49$ and > 0.51 are rather insensitive to increasing $X_0(\text{H}_2)$ from 0.3 to 0.6, but the $\{\text{CH}(\text{X}, v = 0)\}$ and $\{\text{C}_2(\text{a}, v = 0)\}$ values decline by factors of, respectively, ~ 2 and ~ 4 as a result of this decline in $X_{\text{elem}}(\text{C})$, from 0.206 to 0.143.

Figure 5 shows how varying $X_0(\text{H}_2)$ in a $\text{CH}_4/\text{CO}_2/\text{H}_2$ plasma affects the column densities of all the monitored species. These data were all recorded at $z = 10 \text{ mm}$, and with $X_{\text{C}/\Sigma} = 0.5$ (for $\text{OH}(\text{X})$ and $X_{\text{C}/\Sigma} = 0.505$ (for all other species)). Varying

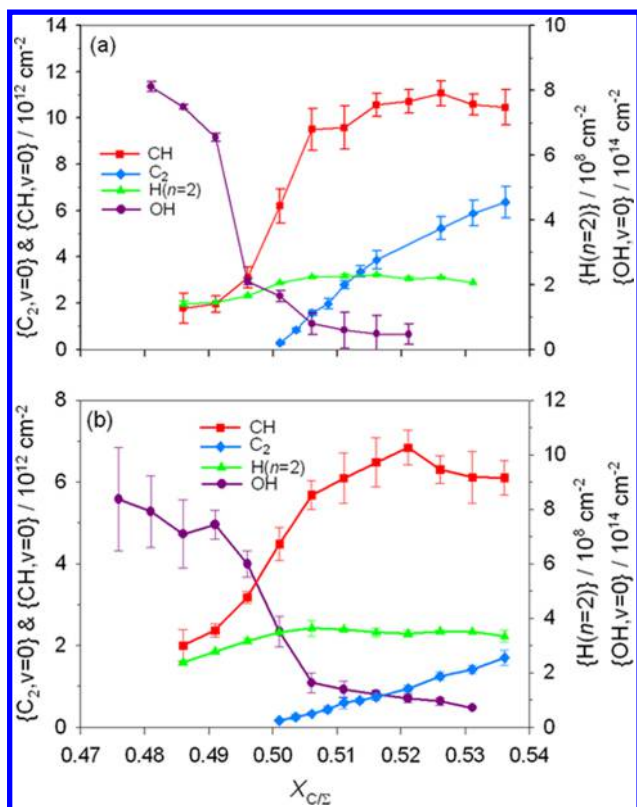


Figure 4. Column densities of $H(n = 2)$ atoms and $C_2(a, \nu = 0)$, $CH(X, \nu = 0)$, and $OH(X, \nu = 0)$ radicals in a $CH_4/CO_2/H_2$ plasma operating at base p , P , and F_{total} measured by CRDS (at $z = 10$ mm) as a function of $X_{C/\Sigma}$ with $X_0(H_2) =$ (a) 0.3 and (b) 0.6.

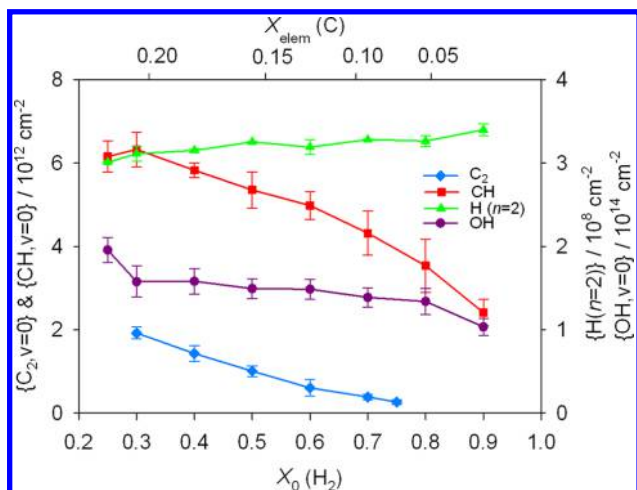


Figure 5. Column densities of $H(n = 2)$ atoms and $C_2(a, \nu = 0)$, $CH(X, \nu = 0)$, and $OH(X, \nu = 0)$ radicals measured by CRDS (at $z = 10$ mm) as a function of $X_0(H_2)$ with $X_{C/\Sigma} = 0.5$ (for OH) and $X_{C/\Sigma} = 0.505$ (for all other species). The corresponding input carbon fractions $X_{elem}(C)$ are shown along the top axis.

$X_0(H_2)$ necessarily changes the elemental carbon, oxygen ($X_{elem}(O)$), and hydrogen ($X_{elem}(H)$) fractions in the input gas mixture. The effect on $X_{elem}(C)$ of increasing $X_0(H_2)$ from 0.25 to 0.9 is shown on the top axis of Figure 5. $X_{elem}(O)$ varies in exactly the same way as $X_{elem}(C)$ when $X_{C/\Sigma} = 0.5$, whereas $X_{elem}(H)$ increases less steeply since it involves contributions from both H_2 and CH_4 . This plot reiterates the comparative insensitivity of $\{H(n = 2)\}$ and $\{OH(X, \nu = 0)\}$ to substantial

changes in $X_0(H_2)$, whereas $\{CH(X, \nu = 0)\}$ and $\{C_2(a, \nu = 0)\}$ decline by factors of, respectively, 2.5 and >10 over the corresponding range.

3.4. Effects of Power, P , and Pressure, p . Figure 6 illustrates the effect that varying (a) the input MW power

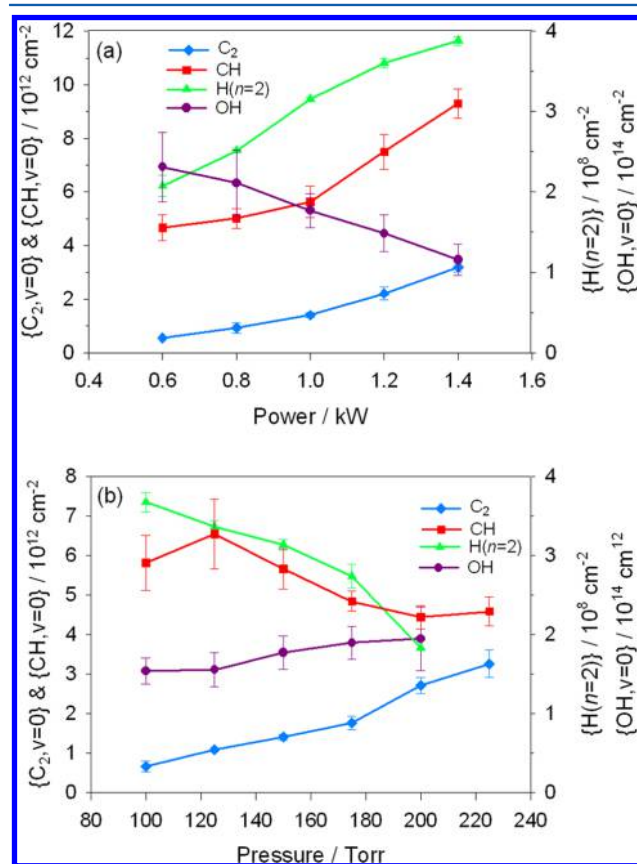


Figure 6. Column densities of $H(n = 2)$ atoms and $C_2(a, \nu = 0)$, $CH(X, \nu = 0)$, and $OH(X, \nu = 0)$ radicals measured by CRDS (at $z = 10$ mm) for gas mixtures involving $X_0(H_2)$ and $X_{C/\Sigma} = 0.5$ (0.505 for $C_2(a)$) as functions of (a) MW power and (b) pressure.

supplied to, and (b) the total pressure of, a $CH_4/CO_2/H_2$ plasma has on each of the measured column densities (at $z = 10$ mm). All of these measurements were made with $X_0(H_2) = 0.3$ and $X_{C/\Sigma} = 0.5$ except those for $C_2(a)$, where signal-to-noise considerations dictated use of $X_{C/\Sigma} = 0.505$. $\{H(n = 2)\}$ and $\{CH(X, \nu = 0)\}$ both increase ~ 2 -fold on raising P from 0.6 to 1.4 kW, $\{C_2(a, \nu = 0)\}$ rises more steeply, but $\{OH(X, \nu = 0)\}$ falls (by a factor of ~ 2). The pressure range explored in Figure 6b spans $100 \leq p \leq 225$ Torr, i.e., more than doubling the total number density, yet this increase is seen to cause a ~ 2 -fold reduction in $\{H(n = 2)\}$, to have rather little effect on $\{CH(X, \nu = 0)\}$ or $\{OH(X, \nu = 0)\}$, and to cause a significant (~ 4 -fold) increase only in the case of $\{C_2(a, \nu = 0)\}$.

4. MODELING THE PLASMA-CHEMICAL KINETICS, PLASMA PARAMETERS, AND SPECIES DISTRIBUTIONS IN MW-ACTIVATED C/H/O MIXTURES

4.1. 2-D(r, z) Model. Many details of the 2-D(r, z) model used to describe essential processes occurring in the MW PECVD reactor have been reported previously.¹⁸ The model assumes cylindrical symmetry, with coordinates r (the radial

distance from the center axis of the reactor) and z (the axial distance from the substrate center), a substrate diameter of 3 cm, and a reactor radius, $R_r = 6$ cm, and height, $h = 6.2$ cm. The set of nonstationary conservation equations for mass, momentum, energy, and species concentrations are solved numerically throughout the entire reactor volume in order to describe the following plasma activation processes: gas heating, heat and mass transfer, species and thermal diffusion, ambipolar diffusion of charged species, gas-surface processes (i.e., diamond deposition and loss/production of radicals, ions, and electrons), and the plasma-chemical kinetics (which requires calculation of the nonequilibrium electron energy distribution function (EEDF)) for a range of C/H/O reactive mixtures and plasma conditions.¹⁸ The volume V in which MW power is absorbed is incorporated as a parameter, guided by experimental absorption and OES data, thereby allowing estimation of the reduced electric field (E/N) and the electron temperature (T_e) in the plasma region for any given value of P . The core plasma region for base conditions ($P = 1$ kW, $p = 150$ Torr, $X_0(\text{CH}_4) = X_0(\text{CO}_2) = 0.35$, $X_0(\text{H}_2) = 0.3$) was determined as $0 \leq r \leq R_{pl} \approx 34$ mm in the radial direction and $0 < z < H_{pl} \approx 16$ mm in the axial direction, with the point $r = 0$, $z = 0$ defining the center of the substrate surface. T_e was assumed near constant within this plasma region, declining by $\sim 3\%$ with increasing z ; typical values for T_e were ~ 1 eV and for the averaged $E/N \sim 35\text{--}40$ Td. The ion temperature (T_{ion}) for the present plasma conditions is close to T_{gas} .

The gas-phase chemistry and thermochemical input for C/H/O mixtures is largely from refs 35–38, supplemented by ion chemistry and kinetic data for the various electron-molecule processes from refs 18 (and references therein), 39, and 40. The C/H/O plasma-chemical kinetics mechanism includes >500 direct and reverse reactions for 50 neutral (C, CH, $^3\text{CH}_2$, $^1\text{CH}_2$, CH_3 , CH_4 , $\text{C}_2(\text{X})$, $\text{C}_2(\text{a})$, C_2H_y ($y = 1\text{--}6$), C_3H_y ($y = 0\text{--}4$), C_4H_y ($y = 0\text{--}2$), C_6H_5 , C_6H_6 ; H, H_2 ($v = 0, 1, 2$), CO ($v = 0, 1, 2$), H_xCO ($x = 1\text{--}3$), CO_2 , $\text{H}_x\text{C}_y\text{O}$ ($x = 0\text{--}2$, $y = 2, 3$); O, O_2 , OH, H_2O , HO_2) species, electronically excited atoms H($n = 2, 3$) and molecules H_2^* , $\text{CO}(\text{a})$, and 10 charged species (electrons, and H^+ , H_2^+ , H_3^+ , C_2H_2^+ , C_2H_3^+ , CO^+ , HCO^+ , CO_2^+ , and H_3O^+), as detailed in the Supporting Information. Negative ions, e.g., C_2H^- , are not considered since the balance of dissociative attachment/collisional detachment processes under the present process conditions ensures that the concentrations of such species are orders of magnitude lower than the electron density.

Most of the 2-D model calculations were performed for base reactor parameters ($P = 1$ kW, $p = 150$ Torr, $F_{total} = 500$ sccm) and mixtures comprising $X_0(\text{H}_2) = 0.3$, $X_0(\text{CH}_4)$ values of, respectively, 0.3, 0.35, and 0.4, and the balance CO_2 . These were chosen to allow investigation of changes in the diamond deposition process across the H–CO tie-line (i.e., $X_{C/\Sigma} = 0.5$ in Figure 1), from oxygen-rich ($X_{C/\Sigma} \approx 0.47$) to carbon-rich ($X_{C/\Sigma} \approx 0.54$). Further calculations were undertaken for $X_0(\text{H}_2) = 0.95$, with $X_0(\text{CH}_4)$ values of, respectively, 0.0255 and 0.0285 and the balance CO_2 in order to explore the effects of varying $X_0(\text{H}_2)$ and of varying $X_{C/\Sigma}$ at high $X_0(\text{H}_2)$. Calculations were also run for a 41.2% $\text{CO}/58.8\%$ H_2 mixture (i.e., a mixture involving the same base C/H/O ratio) at the same P , p , and F_{total} to probe the sensitivity to choice of source gas. Many effects need to be considered in any realistic simulation of these reactive C/H/O mixtures, e.g., changes in diffusion and thermal conduction coefficients and in the ion chemistry and electron kinetics with changes in mixture composition.

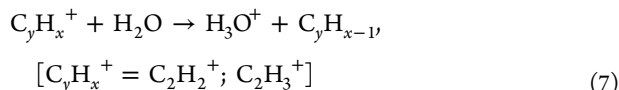
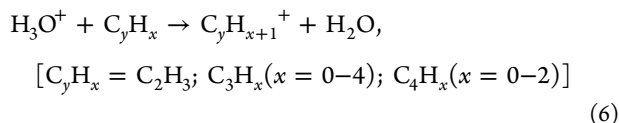
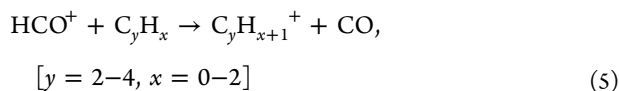
4.2. Plasma Parameters, Power Utilization, Ion Chemistry, and the Ionization–Recombination Balance.

The plasma-chemical and electron kinetics and the power absorption pathways in the present C/H/O mixtures have much in common with those prevailing in the C/H mixtures studied previously.¹⁸ The 2-D model returns the following parameters for the base $\text{CH}_4/\text{CO}_2/\text{H}_2$ plasma: power density $P/V \approx 15\text{--}20$ W cm^{-3} , plasma volume $V \approx 60$ cm^3 , maximal electron densities $n_e \approx 1.35 \times 10^{11}$ cm^{-3} , electron temperatures $T_e \approx 1.06$ eV, and gas temperatures $T_{gas} \approx 3000$ K. The major fraction (>78%) of the MW power absorbed by the electrons is partitioned into vibrational (i.e., $E \rightarrow V$) and rotational (i.e., $E \rightarrow R$) excitation of (mainly) CO and H_2 . Other processes of note occurring at the plasma center include elastic collisions of electrons with H_2 , H, and CO (which account for $\sim 3.5\%$ of the total power consumption), electron impact induced dissociation of H_2 (consuming $\sim 0.37\%$ of the total power), and electronic excitation (mainly to the metastable $\text{a}^3\Pi$ state of CO at $E' = 6.04$ eV), which accounts for $\sim 17.5\%$ of the absorbed power. $\text{CO}(\text{a}^3\Pi)$ molecules are efficiently quenched in collisions with CO and H_2 .⁴¹ In the case of H_2 , interaction with $\text{CO}(\text{a}^3\Pi)$ can lead to dissociation:⁴¹ this constitutes an additional H atom source (indeed, the dominant source in cooler plasma regions with $T_{gas} < 2600$ K). Fast $V \rightarrow T$ and $R \rightarrow T$ energy transfer from the rovibrationally excited H_2 and CO through collision with H atoms results in translational excitation of the latter, which then dissipates into gas heating.

The input power transferred from the electrons to the gas dissipates further by (i) thermal conduction to the reactor walls and (ii) chemical conversions and radiation losses. Representative values for plasmas with $X_0(\text{H}_2) = 0.3$ and $X_{C/\Sigma} = 0.47\text{--}0.54$ that illustrate the relative importance of the various loss processes within (i) are $\sim 14\text{--}17\%$ to the cylinder sidewalls, $\sim 41\text{--}44\%$ to the base plate, $\sim 21\text{--}24\%$ to the substrate and substrate holder, and $\sim 3.3\text{--}5\%$ to the top window. Some 13–17% of the total input power is dissipated via pathway (ii), the majority (>90%) of which is used in thermal dissociation of H_2 . The resulting H atoms play pivotal roles in initiating chemical processing of the C/H/O mixture, in the diamond growth process, and in substrate heating (by H atom adsorption on radical surface sites). As in C/H/Ar plasmas,²³ thermal conduction is calculated to make the greatest contribution to substrate heating; the present modeling of $X_0(\text{H}_2) = 0.3$ and $X_{C/\Sigma} = 0.47\text{--}0.54$ plasmas suggests that H atom adsorption on radical surface sites accounts for only 21–31% of the total ($\sim 22\text{--}25$ W cm^{-2}) power density loading to the substrate.

The main ion forming process in the present C/H/O mixtures is electron impact ionization of the more abundant species, i.e., CO, H_2 , H, C_2H_2 , and H_2O . This production is balanced by dissociative recombination of the dominant ions with electrons. C_yH_x^+ hydrocarbon ions are the most abundant ions in a carbon rich plasma (C_2H_2^+ and C_2H_3^+ in the present scheme, as in dilute C/H plasmas¹⁸), whereas H_3O^+ ions are dominant in the oxygen rich plasma. Under base conditions ($X_{C/\Sigma} = 0.5$), C_2H_2^+ ions are dominant in the plasma center, but H_3O^+ is the dominant ion toward the plasma edge. The dominance of particular ions, and their distributions, are very sensitive to the local $[\text{C}_y\text{H}_x]/[\text{H}_2\text{O}]$ (i.e., $[\text{C}_2\text{H}_2]/[\text{H}_2\text{O}]$) concentration ratio, as a result of the following groups of ion conversion reactions:³⁹





that encourage the (generally irreversible) cycling of $\text{CO}^+ \rightarrow \text{HCO}^+ \rightarrow \text{C}_y\text{H}_x^+$ and/or H_3O^+ (reactions 2–5), $\text{H}_3\text{O}^+ \rightarrow \text{C}_y\text{H}_{x+1}^+$ (reaction family 6), and $\text{C}_y\text{H}_x^+ \rightarrow \text{H}_3\text{O}^+$ (reactions 7).

Thus, we see that the equilibrium of charged species shifts in favor of H_3O^+ with increasing $[\text{H}_2\text{O}]$ and toward C_yH_x^+ if the hydrocarbon concentration is increased. If the ion–electron recombination coefficients β for the various ions were all similar, then the change in dominant ion would be unimportant. However, the calculated rate coefficient for $e\text{-H}_3\text{O}^+$ recombination ($10^{-8} \text{ cm}^3 \text{ s}^{-1}$ for the present EEDF, assuming literature cross-section values⁴²) is almost an order of magnitude smaller than the recombination coefficients for hydrocarbon ions. This difference may lead to unusual effects, such as the nonuniform plasma density distributions predicted for the $X_{\text{C}/\Sigma} = 0.5$ mixture, wherein n_e is predicted to maximize away from the plasma core, i.e., nearer the plasma edge, where n_e is close to the concentration of the (more stable) H_3O^+ ions (Figure 7c). Typical values for the total ionization (and recombination) rates in the plasma core are 2.5×10^{14} (for $X_{\text{C}/\Sigma} = 0.47$), 3.5×10^{14} (for $X_{\text{C}/\Sigma} = 0.5$), and $\sim 10^{15} \text{ cm}^{-3} \text{ s}^{-1}$ (for $X_{\text{C}/\Sigma} = 0.54$). For $X_{\text{C}/\Sigma} = 0.47$ and 0.5, more than half of the ion production is from electron impact ionization of CO (ionization potential, $I(\text{CO}) \approx 14 \text{ eV}$), with the remainder from ionization of H_2 , H, and either H_2O (for $X_{\text{C}/\Sigma} = 0.47$) or C_2H_2 (for $X_{\text{C}/\Sigma} = 0.5$). For $X_{\text{C}/\Sigma} = 0.54$, as in a dilute C/H plasma,¹⁸ ion production is dominated by electron impact ionization of C_2H_2 ($I(\text{C}_2\text{H}_2) \approx 11.4 \text{ eV}$).

4.3. Essential Conversion Mechanisms in MW-Activated C/H/O Mixtures. The spatially resolved mole fraction plots shown in Figure 7a,b illustrates the progressive conversion of the 35% $\text{CH}_4/35\% \text{ CO}_2/30\% \text{ H}_2$ feed gas mixture (which survives only in the cool periphery of the reactor) into a C/H/O mixture dominated by two species, H_2 and CO, throughout the remainder of the reactor volume. Conduction coefficients (λ) for the equivalent 41.2% CO/58.8% H_2 mixture approximated from literature data⁴³ as $\lambda[\text{W cm}^{-1} \text{ K}^{-1}] = 5 \times 10^{-6} \times T_{\text{gas}}^{0.85}$ have thus been used in the present calculations. The λ values for oxygen rich ($X_{\text{C}/\Sigma} = 0.47$)/carbon rich ($X_{\text{C}/\Sigma} = 0.54$) mixtures are, respectively, $\sim 3\%$ smaller/larger. As is also evident from Figure 7c, T_{gas} reaches $\sim 3000 \text{ K}$ in the plasma core, and n_e is typically $\sim 10^{11} \text{ cm}^{-3}$ (with H_3O^+ and C_2H_2^+ as the dominant ions). The unusual off-axis maximum predicted for n_e is a consequence of the distribution of counter-cations (C_2H_2^+ is dominant in the plasma core, whereas H_3O^+ dominates at the plasma edge). This off-axis maximum (which is prominent in the calculated n_e distribution but barely discernible in the T_{gas} profile) is specific to the base mixture

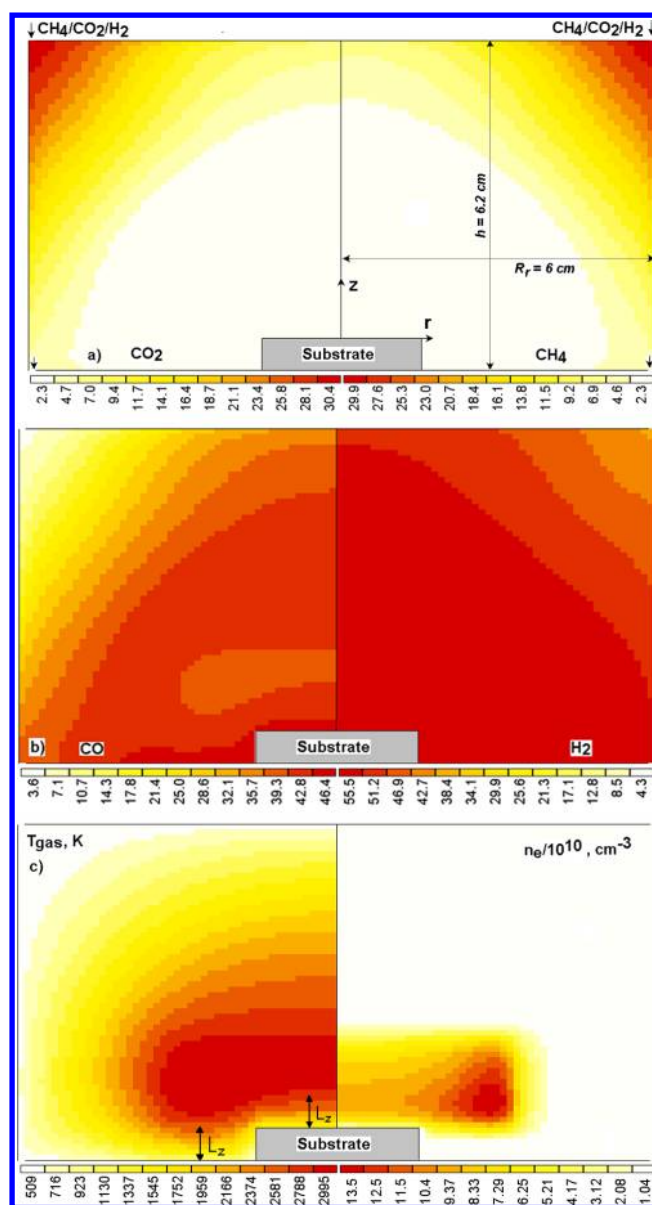


Figure 7. Calculated 2-D(r,z) distributions of CO_2 , CH_4 , CO, and H_2 mole fractions (in %), T_{gas} , and n_e in a 35% $\text{CH}_4/35\% \text{ CO}_2/30\% \text{ H}_2$ gas mixture (i.e., $X_{\text{C}/\Sigma} = 0.5$) operating at base reactor conditions ($P = 1 \text{ kW}$, $p = 150 \text{ Torr}$). The reactor radius R_r and height h are 6 and 6.2 cm, respectively. Given the assumed cylindrical symmetry, only half (in the radial direction) of each 2-D distribution is displayed here and in Figures 9, 10, and 11.

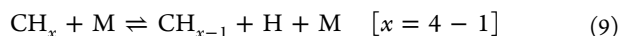
($X_{\text{C}/\Sigma} = 0.5$) and not evident for $X_{\text{C}/\Sigma} = 0.47$ or $X_{\text{C}/\Sigma} = 0.54$, or in the modeling of the 41.2% CO/58.8% H_2 input gas mixture.

As with the C/H mixtures investigated previously,^{18,44} the 2-D modeling allows identification of dominant conversion processes in C/H/O gas mixtures in different regions of the reactor, the cool regions near the gas inlets (with $T_{\text{gas}} < 1400\text{--}1500 \text{ K}$), the hot plasma region ($T_{\text{gas}} \approx 2600\text{--}3000 \text{ K}$, the localization of which is evident from the T_{gas} (and n_e) distributions in Figure 7c), and the peripheral region (the annular shell around the plasma region). The input source gases are dominant in the cool region, where their decomposition is hampered by the relatively low T_{gas} and low H atom concentrations, $[\text{H}]$.

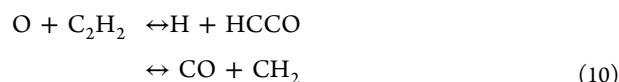
T_{gas} and $[H]$ span the respective ranges $\sim 1500\text{--}2500$ K and $\sim 2 \times 10^{14}\text{--}2 \times 10^{16}$ cm^{-3} in the peripheral region as a result of, respectively, conduction and diffusional transfer from the plasma region. These values are sufficient to ensure near total decomposition of the input CH_4 and CO_2 . The main routes to hydrocarbon decomposition are H-shifting reactions



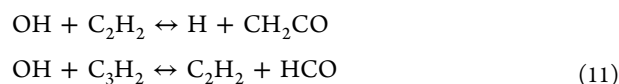
and thermal decomposition



where M is a third body. As for C/H mixtures,^{18,19,42} addition reactions can then lead to heavier hydrocarbon species, i.e., $\text{C}_1\text{H}_x \leftrightarrow \text{C}_2\text{H}_x \leftrightarrow \text{C}_3\text{H}_x$, in both the plasma and peripheral regions, and to yet heavier C_yH_x [$y > 3$] hydrocarbons (e.g., C_6H_6) and soot particles in the latter. In C/H/O mixtures, however, there is an important alternative process: loss of hydrocarbon species via reaction with oxygen-containing species, mainly OH and O, e.g.,



and



all of which lead ultimately to the most stable end-point species, CO.

In parallel with the processing of the hydrocarbons, the input CO_2 is decomposed mainly by reaction with H atoms



This fast reaction (the forward and reverse reaction rates $R_{(\pm 12)}$ both approach 10^{19} cm^{-3} s^{-1} under the prevailing process conditions) yields stable CO products but is also a primary source of an oxygen-containing reactant, OH. Most of these OH radicals are converted to (more stable) H_2O molecules via

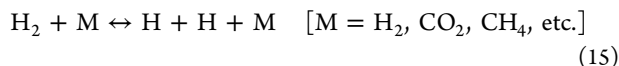


the forward and reverse reaction rates for which approach $R_{(\pm 13)} \approx 2 \times 10^{20}$ cm^{-3} s^{-1} . They also serve as a source of O atoms, however, via the reaction

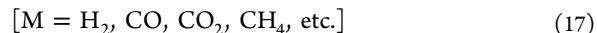
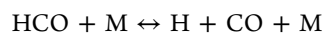


with reaction rates as high as $R_{(14)} \approx 10^{19}$ cm^{-3} s^{-1} .

As with the CH_x and C_2H_x families in C/H plasmas,^{2,3} H-shifting and/or H-addition reactions ensure near-equilibrium distributions inside other groups of species within C/H/O plasmas, e.g., OH_x [$x = 0\text{--}2$], H_xCO [$x = 0\text{--}3$], and H_xC_yO [$x = 0\text{--}2$, $y = 2,3$]. The presence of any translationally hot H atoms could skew these equilibria, enhancing the relative rates of reactions with a barrier, e.g., the endothermic reaction (–13) (for which $\Delta H \approx +0.6$ eV) in favor of OH. The H atoms are produced in the hot plasma region by thermal dissociation of H_2



The direct reaction rate $R_{(15)}$ reaches 10^{19} cm^{-3} s^{-1} at $T_{\text{gas}} \approx 3000$ K. H_2 dissociation in the case that $\text{M} = \text{CO}$ is more complex, involving the (marginally less efficient) two-step process



The calculated rate of electron impact induced dissociation of H_2 never exceeds 10^{17} cm^{-3} s^{-1} , so this plasma source of H atoms is uncompetitive (cf. the thermal source (i.e., $R_{(15)} - R_{(-15)}$)) wherever $T_{\text{gas}} > 2600$ K, i.e., in the hot plasma region.

H atoms formed in the hot plasma region activate the gas-surface reactions that lead to diamond growth on the substrate and diffuse into the peripheral region where they are consumed in driving the various reaction sequences outlined above. The net effect of all of the plasma-chemical mechanisms captured by the 2-D model is illustrated in Figure 8, which shows the

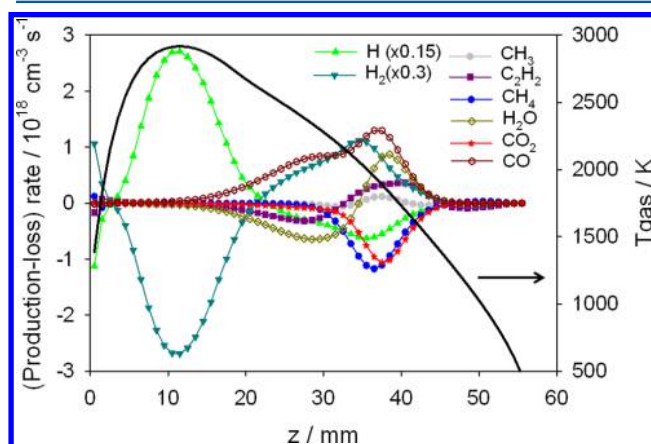


Figure 8. Calculated z -dependence (at $r = 0$) of T_{gas} and of the (production–loss) rates for selected species in a 35% CH_4 /35% CO_2 /30% H_2 gas mixture operating at base reactor conditions ($P = 1$ kW, $p = 150$ Torr). Note that the H and H_2 rates displayed in the plot have been reduced to allow the z -dependence of all other rates to be observed more clearly.

calculated z -dependent profiles of $T_{\text{gas}}(r = 0, z)$ and of the (production–loss) rates for H atoms, H_2 , CH_3 , CH_4 , C_2H_2 , H_2O , CO_2 , and CO at $r = 0$ for the base $\text{CH}_4/\text{CO}_2/\text{H}_2$ gas mixture. Such plots clearly reveal and distinguish the hot plasma ($z < 2.1$ cm), peripheral ($2.1 < z < 4.5$ cm), and cold ($z > 4.5$ cm) regions. The present modeling also reveals a very compressed replica of the peripheral region (in the sense of the prevailing chemical conversions) in the near substrate region ($0 < z < 0.3$ cm), as noted in previous studies of MW-activated C/H mixtures.⁴⁴

Given the main blocks of the C/H/O mechanism described above, it is possible to understand and explain key features of the calculated 2-D(r, z) species distributions for the three $\text{CH}_4/\text{CO}_2/\text{H}_2$ gas mixtures: $X_0(\text{H}_2) = 0.3$ and $X_{\text{C}/\Sigma} = 0.47, 0.5$, and 0.54 . Figure 9 shows how the calculated spatial distributions of CH_x and C_2H_x species (as exemplified by $X(\text{CH})$ and $X(\text{C}_2\text{H}_2)$) evolve upon moving across the H–CO tie-line from an oxygen-rich (Figure 9a, $X_{\text{C}/\Sigma} = 0.47$) to a carbon-rich mixture (Figure 9c, $X_{\text{C}/\Sigma} = 0.54$). These plots clearly show the depletion of hydrocarbons in the plasma region at $X_{\text{C}/\Sigma} = 0.47$ (Figure 9a), as a result of their efficient conversion to CO when oxygen-containing radicals (O, OH) are in excess. The spatial distribution of $X(\text{CH})$ (and $X(\text{C}_2)$, etc.) is predicted to evolve from an annular shell (Figure 9a) through a toroidal profile

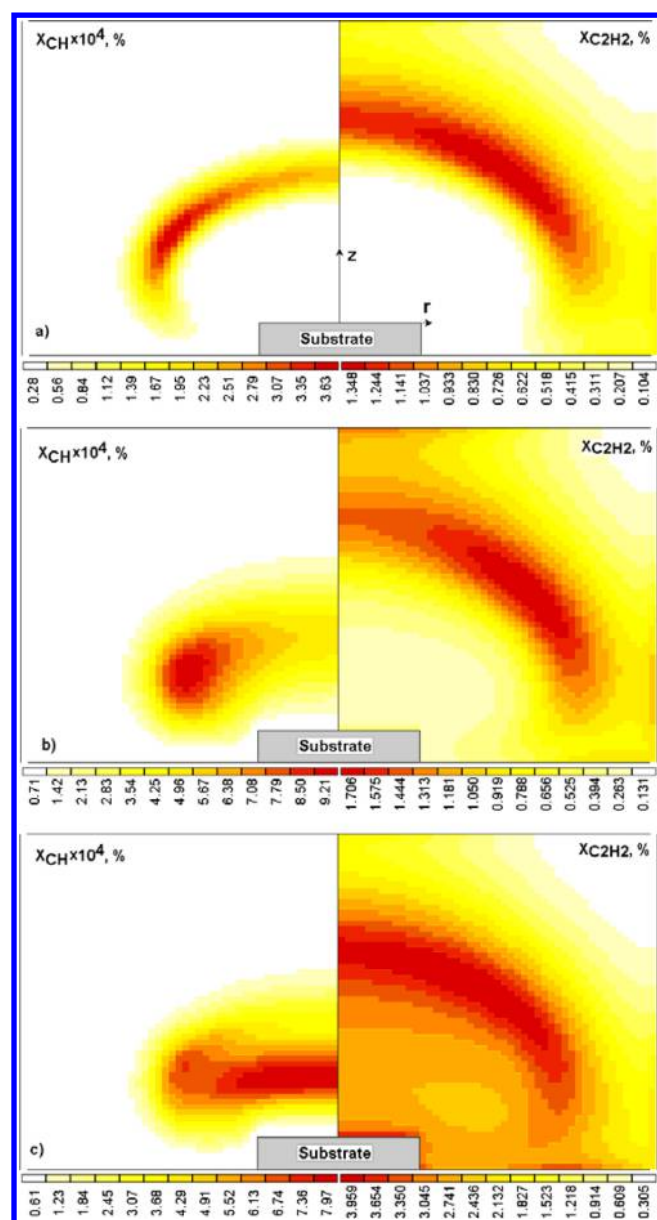


Figure 9. Calculated 2-D(r,z) distributions of CH and C_2H_2 mole fractions (in %) for base reactor conditions ($P = 1$ kW, $p = 150$ Torr) and three different input mixtures: $X_0(H_2) = 0.3$ and $X_{C/\Sigma} =$ (a) 0.47, (b) 0.5, and (c) 0.54.

(Figure 9b, $X_{C/\Sigma} = 0.5$) to an oblate cylinder (Figure 9c) with increasing hydrocarbon fraction.

The calculated spatial distributions of H_xO [$x = 0-2$] mole fractions vary in the opposite way, as illustrated for the case of $X(OH)$ and $X(H_2O)$ in Figure 10. H_xO species are depleted in the plasma region at $X_{C/\Sigma} = 0.54$ (Figure 10c), as a result of their efficient conversion to CO via reaction with hydrocarbons (reactions 10 and 11). The changes in the shape of the $X(OH)$ (and $X(O)$) distributions upon decreasing $X_{C/\Sigma}$ from 0.54 \rightarrow 0.47 essentially mimic the calculated changes in the $X(CH)$ distribution upon increasing $X_{C/\Sigma}$ over the same range. The left-hand panels in Figures 10b and 7c show the regions predicted to make the greatest contribution to the average $T_{rot}(OH)$ under base conditions. These provide a plausible explanation for the measured variations in $T_{rot}(OH(X))$ (section 3.1) and, particularly, the at first sight surprisingly high $T_{rot}(OH(X)) \approx$

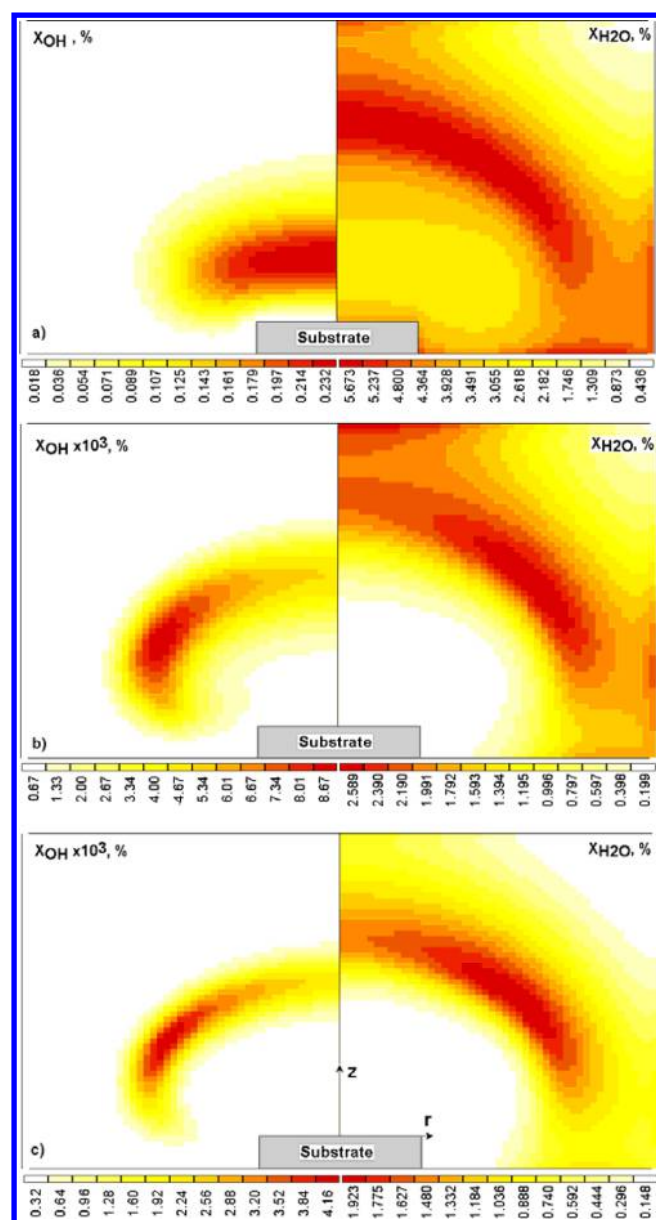


Figure 10. Calculated 2-D(r,z) distributions of OH and H_2O mole fractions (in %) for base reactor conditions ($P = 1$ kW, $p = 150$ Torr) and three different input mixtures: $X_0(H_2) = 0.3$ and $X_{C/\Sigma} =$ (a) 0.47, (b) 0.5, and (c) 0.54.

2400 K value determined at $z = 2$ mm (cf. the calculated $T_{gas}(z = 2$ mm, $0 < r < 15$ mm) ≈ 2000 K above the substrate and $T_{gas}(z = 2$ mm, $32 < r < 36$ mm) $\approx 2200-2500$ K in the regions of predicted maximal $[OH(X)]$). For all mixtures studied ($X_{C/\Sigma} = 0.47-0.54$), the 2-D calculations predict significant production of C_2H_2 and H_2O in the annular shell around the plasma region, leading to steady-state mole fractions of several percent in each case. The importance of this finding is discussed below.

4.4. Diamond Deposition from C/H/O Mixtures and the Dependence on Choice of Feed Gas: Hidden Subtleties within the Bachmann Diagram. The spatially resolved processing of $CH_4/CO_2/H_2$ mixtures in MW PECVD reactors revealed by the present 2-D modeling and the realization of annular shells of C_2H_2 and H_2O (and CH_3 , as in a C/H plasma¹⁸) density around the hot plasma zone has

Table 2. Gas Temperatures (T_{gas}/K) and Selected Species Concentrations (in cm^{-3}) (a) above the Substrate Center (at $r = 0$, $z = 0.5$ mm) and (b) in the Hot Plasma Core ($r = 0$, $z = 9.5$ mm) Returned by the Present 2-D Modelling for a Range of C/H/O Gas Mixtures

(a)							
feed gas	30% CH ₄ /40% CO ₂ / 30% H ₂	35% CH ₄ /35% CO ₂ / 30% H ₂	40% CH ₄ /30% CO ₂ / 30% H ₂	2.55% CH ₄ /2.45% CO ₂ / 95% H ₂	2.85% CH ₄ /2.15% CO ₂ / 95% H ₂	41.2% CO/58.8% H ₂	
T_{gas} (K)	1460	1385	1469	1273	1272	1385	
H	1.27×10^{16}	9.23×10^{15}	8.89×10^{15}	6.22×10^{15}	6.03×10^{15}	1.15×10^{16}	
CH ₃	8.28×10^{11}	2.55×10^{13}	4.85×10^{13}	1.03×10^{14}	1.15×10^{14}	9.73×10^{12}	
³ CH ₂	2.44×10^{10}	1.92×10^{11}	2.58×10^{11}	2.44×10^{11}	2.55×10^{11}	1.24×10^{11}	
¹ CH ₂	5.55×10^8	7.37×10^9	1.77×10^{10}	6.94×10^9	7.48×10^9	3.24×10^9	
CH	3.09×10^9	1.44×10^{10}	1.63×10^{10}	7.01×10^9	7.06×10^9	1.08×10^{10}	
C	1.25×10^{11}	1.88×10^{11}	9.92×10^{10}	2.84×10^{10}	2.52×10^{10}	3.39×10^{11}	
C ₂ (a)	2.36×10^4	5.93×10^7	1.12×10^9	1.21×10^7	1.75×10^7	5.36×10^6	
C ₂ (X)	1.19×10^3	1.54×10^7	3.53×10^8	1.20×10^6	1.44×10^6	1.07×10^6	
C ₂ H	1.42×10^6	3.13×10^{10}	6.71×10^{11}	8.34×10^9	1.03×10^{10}	2.05×10^9	
C ₂ H ₂	4.40×10^{10}	2.82×10^{15}	3.38×10^{16}	4.05×10^{15}	5.16×10^{15}	1.68×10^{14}	
C ₂ H ₃	5.51×10^7	4.07×10^{12}	3.25×10^{13}	7.57×10^{12}	9.51×10^{12}	2.58×10^{11}	
C ₂ H ₄	4.35×10^8	5.06×10^{13}	3.62×10^{14}	2.48×10^{14}	3.20×10^{14}	2.95×10^{12}	
C ₂ H ₅	5.25×10^5	1.84×10^{10}	9.23×10^{10}	1.66×10^{11}	2.15×10^{11}	1.13×10^9	
C ₂ H ₆	8.86×10^6	2.85×10^{10}	7.82×10^{10}	1.23×10^{12}	1.61×10^{12}	2.78×10^9	
C ₃	7.36×10^7	1.41×10^{13}	6.88×10^{13}	2.61×10^{12}	3.21×10^{12}	1.08×10^{12}	
C ₃ H	4.88×10^5	1.32×10^{11}	8.29×10^{11}	4.43×10^{10}	5.76×10^{10}	9.04×10^9	
C ₃ H ₂	1.50×10^8	6.92×10^{13}	4.29×10^{14}	6.88×10^{13}	9.28×10^{13}	4.25×10^{12}	
C ₃ H ₃	8.00×10^5	3.62×10^{11}	4.22×10^{12}	4.38×10^{11}	6.07×10^{11}	1.97×10^{10}	
C ₄	0.24	3.92×10^5	2.99×10^7	2.72×10^4	3.69×10^4	1.20×10^4	
C ₄ H	1.20×10^1	5.98×10^7	5.96×10^9	1.40×10^7	2.01×10^7	1.23×10^6	
C ₄ H ₂	1.75×10^5	3.13×10^{12}	1.91×10^{14}	4.11×10^{12}	6.09×10^{12}	5.20×10^{10}	
C ₆ H ₆	5.30×10^1	6.86×10^9	5.61×10^{11}	3.35×10^{10}	6.37×10^{10}	1.57×10^7	
H($n = 2$)	2.19×10^6	2.61×10^6	4.51×10^6	6.11×10^6	6.04×10^6	2.22×10^6	
H($n = 3$)	8.02×10^4	1.05×10^5	1.69×10^5	3.80×10^5	3.76×10^5	8.26×10^4	
O ₂	7.58×10^{10}	8.17×10^5	4.88×10^4	5.48×10^7	3.12×10^7	1.89×10^6	
H ₂ O	3.73×10^{16}	1.71×10^{14}	2.55×10^{13}	5.01×10^{15}	3.84×10^{15}	3.03×10^{14}	
O	6.13×10^{11}	2.67×10^9	1.56×10^9	2.70×10^9	2.03×10^9	2.83×10^9	
OH	2.44×10^{13}	5.18×10^{10}	1.14×10^{10}	3.33×10^{11}	2.45×10^{11}	1.01×10^{11}	
HCO	9.78×10^{11}	9.47×10^{11}	6.45×10^{11}	2.61×10^{11}	7.68×10^{10}	8.98×10^{11}	
CH ₂ O	1.19×10^{10}	1.01×10^{10}	9.66×10^9	8.41×10^9	4.34×10^9	8.64×10^9	
CH ₃ O	3.86×10^5	2.63×10^4	1.43×10^4	7.34×10^5	6.23×10^5	1.61×10^4	
CO(a)	2.55×10^{10}	3.81×10^{10}	7.50×10^{10}	8.56×10^9	7.93×10^9	2.78×10^{10}	
<i>e</i>	3.82×10^{10}	3.07×10^{10}	7.17×10^{10}	9.40×10^{10}	9.40×10^{10}	3.18×10^{10}	
C ₂ H ₂ ⁺	1.24×10^5	2.47×10^{10}	5.65×10^{10}	1.55×10^{10}	2.41×10^{10}	4.60×10^9	
C ₂ H ₃ ⁺	1.05×10^2	1.11×10^9	1.48×10^{10}	2.56×10^8	3.88×10^8	1.04×10^8	
H ₃ O ⁺	3.82×10^{10}	4.84×10^9	4.28×10^8	7.83×10^{10}	6.95×10^{10}	2.70×10^{10}	
CH ₄	2.36×10^{12}	1.18×10^{14}	1.83×10^{14}	1.29×10^{15}	1.48×10^{15}	4.33×10^{13}	
CO ₂	9.64×10^{15}	4.21×10^{13}	9.71×10^{12}	2.68×10^{13}	1.86×10^{13}	5.39×10^{13}	
CO	4.65×10^{17}	4.69×10^{17}	3.97×10^{17}	2.88×10^{16}	2.60×10^{16}	4.03×10^{17}	
H ₂	4.68×10^{17}	5.65×10^{17}	5.46×10^{17}	1.09×10^{18}	1.10×10^{18}	6.32×10^{17}	
(b)							
feed gas	30% CH ₄ /40% CO ₂ / 30% H ₂	35% CH ₄ /35% CO ₂ / 30% H ₂	40% CH ₄ /30% CO ₂ / 30% H ₂	2.55% CH ₄ /2.45% CO ₂ / 95% H ₂	2.85% CH ₄ /2.15% CO ₂ / 95% H ₂	41.2% CO/58.8% H ₂	
T_{gas} (K)	3071	2898	2899	2805	2796	2947	
H	5.02×10^{16}	3.92×10^{16}	4.49×10^{16}	2.52×10^{16}	2.51×10^{16}	4.76×10^{16}	
CH ₃	4.44×10^{10}	1.64×10^{13}	2.85×10^{13}	8.61×10^{13}	8.93×10^{13}	5.71×10^{12}	
³ CH ₂	1.98×10^{10}	4.20×10^{12}	8.23×10^{12}	7.78×10^{12}	7.95×10^{12}	1.63×10^{12}	
¹ CH ₂	2.33×10^9	4.79×10^{11}	9.42×10^{11}	8.38×10^{11}	8.55×10^{11}	1.90×10^{11}	
CH	1.24×10^{10}	1.69×10^{12}	3.74×10^{12}	1.13×10^{12}	1.15×10^{12}	7.18×10^{11}	
C	3.88×10^{10}	4.10×10^{12}	1.02×10^{13}	1.13×10^{12}	1.15×10^{12}	1.79×10^{12}	
C ₂	4.08×10^6	6.91×10^{11}	1.12×10^{13}	8.63×10^{10}	1.08×10^{11}	4.61×10^{10}	
C ₂ (X)	9.47×10^5	1.64×10^{11}	2.66×10^{12}	2.08×10^{10}	2.61×10^{10}	1.09×10^{10}	
C ₂ H	6.24×10^7	1.77×10^{13}	2.55×10^{14}	6.41×10^{12}	8.15×10^{12}	1.06×10^{12}	
C ₂ H ₂	1.64×10^9	9.67×10^{14}	1.23×10^{16}	1.15×10^{15}	1.50×10^{15}	4.85×10^{13}	
C ₂ H ₃	4.26×10^5	1.80×10^{11}	2.15×10^{12}	3.22×10^{11}	4.03×10^{11}	1.07×10^{10}	

Table 2. continued

feed gas	(b)					
	30% CH ₄ /40% CO ₂ / 30% H ₂	35% CH ₄ /35% CO ₂ / 30% H ₂	40% CH ₄ /30% CO ₂ / 30% H ₂	2.55% CH ₄ /2.45% CO ₂ / 95% H ₂	2.85% CH ₄ /2.15% CO ₂ / 95% H ₂	41.2% CO/58.8% H ₂
C ₂ H ₄	1.25 × 10 ⁵	8.44 × 10 ¹⁰	8.85 × 10 ¹¹	4.51 × 10 ¹¹	5.69 × 10 ¹¹	4.54 × 10 ⁹
C ₂ H ₅	7.05 × 10 ²	1.03 × 10 ⁸	2.85 × 10 ⁸	3.63 × 10 ⁹	3.89 × 10 ⁹	1.10 × 10 ⁷
C ₂ H ₆	2.14 × 10 ¹	4.89 × 10 ⁶	1.29 × 10 ⁷	3.73 × 10 ⁸	4.07 × 10 ⁸	4.98 × 10 ⁵
C ₃	2.46 × 10 ⁴	1.71 × 10 ¹²	5.37 × 10 ¹³	3.65 × 10 ¹¹	4.90 × 10 ¹¹	3.12 × 10 ¹⁰
C ₃ H	3.07 × 10 ²	3.11 × 10 ¹⁰	8.64 × 10 ¹¹	1.66 × 10 ¹⁰	2.24 × 10 ¹⁰	5.42 × 10 ⁸
C ₃ H ₂	1.36 × 10 ⁴	2.23 × 10 ¹²	5.50 × 10 ¹³	3.28 × 10 ¹²	4.45 × 10 ¹²	3.57 × 10 ¹⁰
C ₃ H ₃	1.64 × 10 ³	3.26 × 10 ¹¹	7.13 × 10 ¹²	1.14 × 10 ¹²	1.54 × 10 ¹²	5.15 × 10 ⁹
C ₄	0	6.63 × 10 ⁸	1.34 × 10 ¹¹	5.52 × 10 ⁷	8.98 × 10 ⁷	2.02 × 10 ⁶
C ₄ H	0.10	1.31 × 10 ¹⁰	2.35 × 10 ¹²	3.06 × 10 ⁹	5.04 × 10 ⁹	3.58 × 10 ⁷
C ₄ H ₂	2.48	6.48 × 10 ¹¹	1.04 × 10 ¹⁴	4.90 × 10 ¹¹	8.27 × 10 ¹¹	1.51 × 10 ⁹
C ₆ H ₆	0	2.01 × 10 ⁵	9.42 × 10 ⁷	3.41 × 10 ⁶	6.39 × 10 ⁶	4.30 × 10 ¹
H(<i>n</i> = 2)	4.57 × 10 ⁷	4.09 × 10 ⁷	4.62 × 10 ⁷	1.02 × 10 ⁸	1.02 × 10 ⁸	4.74 × 10 ⁷
H(<i>n</i> = 3)	2.07 × 10 ⁶	2.05 × 10 ⁶	2.12 × 10 ⁶	8.01 × 10 ⁶	8.02 × 10 ⁶	2.21 × 10 ⁶
O ₂	3.71 × 10 ¹²	9.11 × 10 ⁶	1.55 × 10 ⁴	7.22 × 10 ⁸	4.00 × 10 ⁸	5.04 × 10 ⁷
H ₂ O	1.29 × 10 ¹⁶	3.84 × 10 ¹³	1.43 × 10 ¹²	1.34 × 10 ¹⁵	1.02 × 10 ¹⁵	8.41 × 10 ¹³
O	1.54 × 10 ¹⁴	1.58 × 10 ¹¹	7.28 × 10 ⁹	6.47 × 10 ¹¹	4.75 × 10 ¹¹	4.40 × 10 ¹¹
OH	1.07 × 10 ¹⁵	1.74 × 10 ¹²	7.30 × 10 ¹⁰	1.98 × 10 ¹³	1.47 × 10 ¹³	4.37 × 10 ¹²
HCO	1.37 × 10 ¹²	8.83 × 10 ¹¹	7.66 × 10 ¹¹	7.96 × 10 ¹⁰	4.19 × 10 ¹⁰	8.63 × 10 ¹¹
CH ₂ O	3.32 × 10 ¹⁰	2.84 × 10 ¹⁰	2.17 × 10 ¹⁰	1.22 × 10 ¹⁰	7.85 × 10 ⁹	2.65 × 10 ¹⁰
CH ₃ O	3.07 × 10 ⁶	1.99 × 10 ⁶	1.36 × 10 ⁵	1.68 × 10 ⁸	1.29 × 10 ⁸	1.51 × 10 ⁶
CO(a ³ Π)	1.16 × 10 ¹¹	1.14 × 10 ¹¹	1.23 × 10 ¹¹	2.01 × 10 ¹⁰	1.82 × 10 ¹⁰	1.10 × 10 ¹¹
<i>e</i>	1.37 × 10 ¹¹	7.87 × 10 ¹⁰	1.00 × 10 ¹¹	2.76 × 10 ¹¹	2.72 × 10 ¹¹	1.10 × 10 ¹¹
C ₂ H ₂ ⁺	1.41 × 10 ⁶	3.81 × 10 ¹⁰	7.41 × 10 ¹⁰	1.76 × 10 ¹⁰	2.66 × 10 ¹⁰	8.06 × 10 ⁹
C ₂ H ₃ ⁺	9.37	6.30 × 10 ⁹	2.57 × 10 ¹⁰	7.42 × 10 ⁸	1.25 × 10 ⁹	6.00 × 10 ⁸
H ₃ O ⁺	1.37 × 10 ¹¹	3.41 × 10 ¹⁰	1.54 × 10 ⁸	2.57 × 10 ¹¹	2.44 × 10 ¹¹	9.99 × 10 ¹⁰
CH ₄	1.17 × 10 ¹⁰	6.62 × 10 ¹²	1.03 × 10 ¹³	9.49 × 10 ¹³	9.94 × 10 ¹³	2.12 × 10 ¹²
CO ₂	1.57 × 10 ¹⁵	3.97 × 10 ¹²	1.63 × 10 ¹¹	3.25 × 10 ¹²	2.22 × 10 ¹²	6.07 × 10 ¹²
CO	1.94 × 10 ¹⁷	1.95 × 10 ¹⁷	1.74 × 10 ¹⁷	8.10 × 10 ¹⁵	7.32 × 10 ¹⁵	1.53 × 10 ¹⁷
H ₂	2.12 × 10 ¹⁷	2.65 × 10 ¹⁷	2.69 × 10 ¹⁷	4.81 × 10 ¹⁷	4.83 × 10 ¹⁷	2.92 × 10 ¹⁷

direct consequences for the probability of diamond deposition from C/H/O mixtures with elemental compositions close to the H–CO tie-line. Specifically, diffusion of C₂H₂ molecules (present within the annular shell under base conditions at concentrations $\sim 10^{16}$ cm⁻³) into the plasma zone provides the main source of CH_{*x*} [*x* = 0–3] radicals via interconversion between (and fast exchange within) the C₂H_{*y*} and CH_{*x*} families both in the plasma region and immediately above the substrate. A somewhat similar picture of an annular shell of CH₃ radical density and a shell-like/hemispherical distribution of C₂H₂ density was identified in our analysis of MW-activated C/H plasmas, which yielded details of the relevant species interconversions and accounted for the observed insensitivity of the plasma composition to the choice of C/H source gas.^{18,19} In contrast to C/H mixtures, we identify two important behavioral differences in the case of C/H/O mixtures.

First, there is an annular shell of H₂O molecules (comparable to that of C₂H₂, Figures 9 and 10) around the hot plasma region. Diffusional transfer of H₂O into the latter will result in decomposition, thereby constituting a source of OH (and O) radicals. As noted above, these radicals provide a sink for hydrocarbon species, converting them to more stable (in the plasma zone) CO molecules. This sink causes a substantial drop in the densities of C₂H_{*y*} and CH_{*x*} species in the oxygen-rich plasmas, as seen in the CRDS data (Figure 4) and in the OES data reported in the companion article²⁴, and reduces (or even prevents) diamond deposition. This trend is also clearly evident in the 2-D model outputs, e.g., in the calculated

densities of selected species at *z* = 0.5 and 9.5 mm above the substrate for a range of different feed gas mixtures (Table 2).

Second, the realization that annular shells of C₂H₂ and H₂O density around the hot plasma volume are an essential feature in the conversion of a CH₄/CO₂/H₂ mixture into a mixture dominated by CO and H₂ raises the question whether similar annular shells of C₂H₂ and H₂O would arise if an equivalent CO/H₂ mixture was used as source gas. If not, it would imply an important difference in the behaviors of C/H/O and C/H gas mixtures upon MW activation and highlight hidden subtleties within the Bachmann diagram.

Thus, additional 2-D calculations were undertaken for a 41.2% CO/58.8% H₂ feed gas mixture. The calculated maximal gas and electron temperatures ($T_{\text{gas}} \approx 3000$ K and $T_e \approx 1.03$ eV) and electron concentrations ($n_e \approx 1.2 \times 10^{11}$ cm⁻³) are all similar to the corresponding values found with the base CH₄/CO₂/H₂ mixture, but the neutral chemical transformations and radical production rates are very different. The 2-D calculations predict completely different distributions of C₂H₂, H₂O, and of all other species, both with regard to spatial profiles and the absolute values (cf. Figure 11 with Figures 9b and 10b). As in a previous study of DC discharge PECVD from CO/H₂ mixtures,⁴⁵ the primary source of carbon and oxygen containing radicals in the CO/H₂ plasma will be the electron impact dissociation of CO:



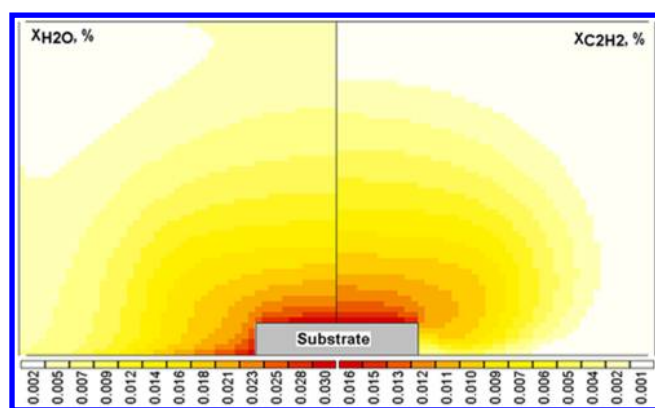
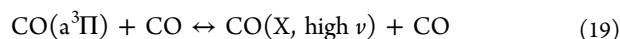
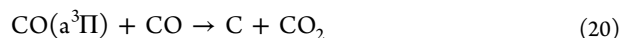


Figure 11. Calculated 2-D(r,z) distributions of H_2O and C_2H_2 mole fractions (in %) for a 41.2% $\text{CO}/58.8\%$ H_2 mixture and base reactor conditions ($P = 1$ kW, $p = 150$ Torr).

Published cross-section data⁴⁶ allow estimation of typical dissociation rate coefficients $k_{18} \approx 2 \times 10^{-13} \text{ cm}^3 \text{ s}^{-1}$ and dissociation rates $R_{(18)} \approx 5 \times 10^{15} \text{ cm}^{-3} \text{ s}^{-1}$ under the present process conditions. The previously noted electron energy transfer channel involving excitation of CO to its $a^3\Pi$ state and subsequent $E \rightarrow V$



and/or reactive



quenching⁴¹ of $\text{CO}(a)$ by CO (and H_2) is important in our plasma environment. Invoking a reactive quenching contribution with rate constant $k_{20} = 2.2 \times 10^{-13} \text{ cm}^3 \text{ s}^{-1}$ (i.e., just $\sim 0.4\%$ of the measured total quenching rate) leads to a 40% (25%) increase in the CH (OH) column densities returned by the 2-D calculations. Any further increase in the assumed k_{20} value results in a CH column density greater than that measured experimentally. Reactions 18 and 20 constitute the main (plasma) source of primary radicals (O and C atoms) in a CO/H_2 mixture, in contrast to the dominant (thermal) source of primary radicals (CH_3 , OH) in $\text{CH}_4/\text{CO}_2/\text{H}_2$ mixtures. Two-dimensional modeling suggests that the subsequent $\text{C} \leftrightarrow \text{CH} \leftrightarrow \text{CH}_2 \leftrightarrow \text{CH}_3 \leftrightarrow \text{CH}_4$, $\text{CH}_{x1} + \text{CH}_{x2} \leftrightarrow \text{C}_2\text{H}_y$, and $\text{O} \leftrightarrow \text{OH} \leftrightarrow \text{H}_2\text{O}$ interconversions yield a distribution of species concentrations within the reactor (Figure 3b and 11) and, particularly, above the substrate center (Table 2) that differs markedly from that obtained with the equivalent 35% $\text{CH}_4/35\%$ $\text{CO}_2/30\%$ H_2 mixture (cf. Figures 3a, 9b, and 10b). Two-dimensional modeling assuming reactions 18 and 20 as the sources of C atoms return a lower diamond deposition rate for the base CO/H_2 plasma ($G \approx 0.8 \mu\text{m h}^{-1}$, cf. $G \approx 1.6 \mu\text{m h}^{-1}$ for the base $\text{CH}_4/\text{CO}_2/\text{H}_2$ mixture), consistent with the scarcity of reports of successful diamond growth from MW-activated CO/H_2 plasmas in Bachmann's overview.¹

By comparing Figure 3a,b, we can note that the measured $\{\text{OH}(X), \nu = 0\}$ values in the 41.2% $\text{CO}/58.8\%$ H_2 plasma are ~ 3 times higher than the model prediction, an observation that may provide further (indirect) evidence for the presence of hot H atoms in the plasma.^{18,19} Reaction 13 is the most important in establishing $[\text{OH}]$ in the hot plasma region. The reverse rate coefficient, $k_{-13} [\text{cm}^3 \text{ s}^{-1}] \approx 6.9 \times 10^{-10} \exp(-12160/T_{\text{gas}})$, is a sensitive function of T_{gas} (or the H atom translational temperature, T_{H} in the case that $T_{\text{H}} > T_{\text{gas}}$). The ~ 3 -fold difference could be eliminated if we assume $T_{\text{H}} \sim 4100$ K in the

expression for k_{-13} instead of $T_{\text{gas}} \approx 3000$ K in the hot plasma core. Recall that, as in our previous studies of MW-activated $\text{C}/\text{H}/\text{Ar}$ plasmas,¹⁹ the present CRDS measurements return Balmer- α line widths, which, if attributed solely to the fine structure splitting and Doppler broadening effects, imply $T_{\text{H}} > T_{\text{gas}}$.

How might such a non-equilibrium situation arise? One possibility could be efficient production of vibrationally excited H_2 and CO molecules at rates comparable to their rates of vibrational \rightarrow translational ($V \rightarrow T$) relaxation. $\text{CO}(a)$ quenching (reaction (19)), electron impact excitation, or other exothermic reactions all might conceivably lead to further H atom heating via $V \rightarrow T$ relaxation processes (see Supporting Information). Though fast, however, (e.g. $k(\text{CO}(\nu = 1) + \text{H} \rightarrow \text{CO}(\nu = 0) + \text{H}_{\text{hot}} 3000 \text{ K}) \sim 2 \times 10^{-10} \text{ cm}^3 \text{ s}^{-1}$ [ref 47]) these processes are still not competitive with the very fast $T \rightarrow T$ exchange between H and H_2 , and between 'light' (H , H_2) and 'heavy' (CO) species. Thus we should expect the translational temperatures of all species to be in local thermal equilibrium. Supporting this view, we note an early coherent anti-Stokes Raman spectroscopy (CARS) study of MW activated CH_4/H_2 plasmas, which determined $T_{\text{vib}}(\text{H}_2)$ values only ~ 200 K higher than the rotational temperature $T_{\text{rot}}(\text{H}_2) \sim T_{\text{gas}}$ (ref 48).

Analysis of the incident laser intensity and the coupling of this radiation into the cavity suggests another plausible explanation for the seemingly anomalous Balmer- α linewidth – namely, partial saturation of the $\text{H}(n = 3 \leftarrow n = 2)$ transition under the prevailing probe conditions. Model calculations suggest that the measured linewidths could be reproduced by invoking a 30% reduction of $[\text{H}(n = 2)]$ due to optical pumping at the Balmer- α line center (and zero reduction when exciting in the wings of the absorption line). Related saturation issues have been recognised previously when monitoring ground state boron atoms in MW activated $\text{B}/\text{H}/\text{Ar}$ and $\text{B}/\text{C}/\text{H}/\text{Ar}$ plasmas.^{21,22} In the present context, such an explanation (if correct) should have negligible impact on any of the reported $\{\text{H}(n = 2)\}$ distributions, but all of the column densities would be under-estimated by $\sim 20\%$.

The greater complexity of the processing of $\text{C}/\text{H}/\text{O}$ gas mixtures revealed by the present modeling has important implications when it comes to comparing 2-D(r,z) model and experimental (i.e., 3-D(r,z,φ), where φ is the azimuthal angle) data, particularly in the case of the $\text{CH}_4/\text{CO}_2/\text{H}_2$ plasmas. The actual PECVD reactor deviates from cylindrical symmetry in as much that the premixed source gas enters through two diametrically opposed $1/4''$ tubes located at $\varphi \approx 45^\circ$ to the probe axis,¹⁹ while the 2-D modeling assumes φ -independent gas entry via a cylindrical ring located at $r = 6$ cm. As Figure 7a,b showed, the calculated CO_2 and CH_4 mole fractions have fallen to values below that of $X(\text{CO})$ and $X(\text{H}_2)$ once the gas has reached ~ 3 cm from the inlet. This suggests that, in the experiment, we actually have two localized regions extending from the respective inlets in which CO_2 and CH_4 are dominant. The combined volume of these two regions is considerably smaller than that of the cylindrically symmetric cloud extending from the inlet ring (of length $2\pi \times 6 \approx 38$ cm) assumed in the 2-D(r,z) model. These differences in the model and experimental reactor geometries and the sensitivity of the various radical densities to the choice of $\text{C}/\text{H}/\text{O}$ source gas, are both envisioned as major contributory factors to the evident discrepancies between the measured and predicted species concentrations.

To investigate this further, additional 2-D calculations have been run in which the process gas is introduced through an orifice located at $z = 6$ cm, $r = 0$, with a cross-section equivalent to the sum of that of the two 1/4" tubes. These calculations also show the CO₂ and CH₄ source gases localized in a roughly conical volume of diameter ~ 6 cm extending from immediately beneath the quartz window for distances $\Delta z_{\text{cone}}[\text{cm}] \approx 1.3 \times (1 - (r/3))$, beyond which their respective densities have each fallen by factors of (at least) ten. Thereafter, the calculations show progressive quasi-cylindrical clouds of CH₃, C₂H₂, CH, and C and, in the case of O containing species, H₂O, OH, and O upon approaching the substrate. These calculations return a more traditional n_e distribution, without any pronounced maximum at the plasma edge, and absolute OH(X), CH(X), and C₂(a) column densities that match more closely with the experimental data. Both 2-D model reactor schemes overestimate (in comparison with experiment or any more realistic 3-D azimuthally asymmetric model) the concentrations of carbon-containing source gases (and hence the H_xO and C_xH_y concentrations) in the gap between the plasma and the top quartz window. Nonetheless, as shown below, the current 2-D modeling with the assumption that the process gas is introduced in a cylindrically symmetric manner (at $r = 6$ cm) does allow us to predict and explain many of the experimentally observed variations in radical concentrations and optical emission intensities, and in plasma parameters, upon changing process conditions.

4.5. Behavior of C/H/O Plasma upon Varying Reactor Parameters: Comparing CRDS Data with the 2-D Model Results. As in previous studies of MW-activated C/H,^{18–20} C/H/B,^{21,22} and C/H/Ar²³ gas mixtures, the 2-D modeling is challenged to explain a plethora of CRDS and OES data for CH₄/CO₂/H₂ (and CO/H₂) plasmas and trends revealed by systematic variation of the process conditions.

4.5.1. Base C/H/O Plasmas. One notable finding (both experimentally and in the 2-D model) regarding the CH₄/CO₂/H₂ plasma is that similar (or even slightly higher) maximal gas temperatures ($T_{\text{gas}} \approx 3000$ K), H atom mole fractions ($X(\text{H}) \approx 8\text{--}10\%$), and CH₃ radical densities in the annular shell around the hot plasma region ($[\text{CH}_3] \approx 10^{15} \text{ cm}^{-3}$) can be achieved using a considerably lower power ($P \approx 1$ kW) than in the case of a C/H plasma ($P \approx 1.5$ kW). The 2-D model operates with plasma volumes $V_{\text{C/H/O}} \approx \pi R_{\text{pl}}^2 H_{\text{pl}} \approx 60 \text{ cm}^3$ and $V_{\text{C/H}} \approx 43 \text{ cm}^3$ and thus with average power densities $P/V \approx 17$ and 35 W cm^{-3} for C/H/O and C/H plasmas, respectively. That the same maximal T_{gas} values are attained with P/V ratios that differ by a factor of 2 can be traced to the very different thermal conductivity coefficients: $\lambda_{\text{C/H/O}} \approx \lambda_{\text{C/H}}/2.3$ for $T_{\text{gas}} \approx 1500\text{--}3000$ K. A similar effect was noted in the case of Ar-rich C/H/Ar plasmas,²³ where a more than 10-fold reduction in P/V (from 35 to 2.2 W cm^{-3}) upon increasing $X_0(\text{Ar})$ from ~ 0.07 to 0.99 resulted in little change in maximal gas temperature ($T_{\text{max}} \approx 3000$ K). A straightforward estimate of T_{max} for the case of a C/H/O (or C/H) plasma sitting on the substrate and base plate (as in Figure 7c) can be obtained from the thermal conduction equation without sources, integrated over the axial gap L_z between the edge of the hot plasma core (with temperature T_{max}) and the nearest cold walls, i.e., particularly the base-plate and substrate:

$$T_{\text{max}} \approx T_{\text{wall}} + \delta PL_z / (S\lambda_{\text{eff}}) \quad (21)$$

$S = \pi R_{\text{pl}}^2 = V/H_{\text{pl}} \approx 40 \text{ cm}^2$ is a characteristic radial cross-section of the plasma region, $\delta \approx 0.65$ is the part of the total

input power transferred to the base-plate and substrate (recall section 4.2), and λ_{eff} is an effective conduction coefficient, $\lambda(T_{\text{wall}}) < \lambda_{\text{eff}} < \lambda(T_{\text{max}})$. If we assume a functional dependence, $\lambda(T_{\text{gas}}) = aT_{\text{gas}}^b$ and $T_{\text{wall}} \ll T_{\text{max}}$, $\lambda_{\text{eff}} \approx \lambda(T_{\text{max}})/(b+1)$. For the water cooled base-plate, with temperature $T_{\text{wall}} \approx 300$ K and $\lambda_{\text{eff}} \approx \lambda(T_{\text{max}} = 3000 \text{ K})/1.85 = 0.0024 \text{ W cm}^{-1} \text{ K}^{-1}$ in the base C/H/O mixture ($b = 0.85$, recall section 4.3), we obtain $L_z \approx 0.45$ cm from eq 21, consistent with the T_{gas} distribution shown in Figure 7c.

Table 2 lists gas temperatures and concentrations of selected species calculated (at $z = 0.5$ and at $z = 9.5$ mm above the substrate center) for a range of C/H/O mixtures including the base CH₄/CO₂/H₂ mixture and the equivalent 41.2% CO/58.8% H₂ mixture, which illustrate compositional differences (e.g., the $[\text{H}]/[\text{CH}_3]$ ratio) that will impact on diamond growth. As with C/H gas mixtures,³ CH₃ is predicted to be the most abundant C₁H_x radical species near the growing diamond surface with the base C/H/O mixture and is assumed to be the main diamond growth species. The predicted CH₃ density is substantially reduced in oxygen-rich C/H/O mixtures with $X_0(\text{H}_2) = 0.3$, and (to a much lesser extent) in the 41.2% CO/58.8% H₂ mixture, but the calculations for $X_0(\text{H}_2) = 0.95$, $X_{\text{C}/\Sigma} = 0.54$ (i.e. 2.85% CH₄/2.15% CO₂), and $X_{\text{C}/\Sigma} = 0.505$ (i.e., 2.55% CH₄/2.45% CO₂) predict CH₃ concentrations and H atom mole fractions similar to those found with standard CH₄/H₂ mixtures (e.g., 4.4% CH₄/H₂, $P = 1\text{--}1.5 \text{ kW}$ ^{18,20}). The 2-D modeling also predicts enhanced production, and survival, of larger hydrocarbon species like C₃H₂, C₃H₃, C₄H₂, and C₆H₆ in the cooler regions of carbon-rich C/H/O mixtures. An increased density of such species would be expected to encourage soot formation,³⁶ in line with experimental observation.

The 2-D modeling of MW-activated CH₄/CO₂/H₂ plasmas using the foregoing plasma parameters and plasma-chemical conversions fails to reproduce the detailed z -dependent $\{\text{CH}(X), \nu = 0\}$ and $\{\text{OH}(X), \nu = 0\}$ distributions determined experimentally, for reasons discussed above, but generally succeeds in reproducing (qualitatively and, in many cases, quantitatively) much of the experimental data (from both CRDS and OES). For example, the 2-D model predicts $\{\text{CH}(X), \nu = 0\}$ values of $1.90 \times 10^{12} \text{ cm}^{-2}$ (at $X_{\text{C}/\Sigma} = 0.47$), $1.58 \times 10^{13} \text{ cm}^{-2}$ ($X_{\text{C}/\Sigma} = 0.5$), and $1.88 \times 10^{13} \text{ cm}^{-2}$ ($X_{\text{C}/\Sigma} = 0.54$) at $z = 9.5$ mm and $X_0(\text{H}_2) = 0.3$, in good absolute accord with the experimental data (Figure 4a). The model column densities (e.g., $\{\text{CH}(X), \nu = 0\}$) are calculated at the z of interest by integrating over the reactor diameter, i.e., $\int [\text{CH}(X), \nu = 0, r] dr$. The experimental column densities, in contrast, are derived from the absorbance associated with a particular spectral line, originating from a particular rotational level J , which contains a (T_{gas} dependent) fraction $p_{\text{line}}(J)$ of the total population as described in section 3.2, i.e., from the integral $\int [\text{CH}(X), \nu = 0, J, r] dr = \int p(J) [\text{CH}(X), \nu = 0, r] dr$. The same integral could be calculated in the model, but as Table 1 showed, the $p_{\text{line}}(J)$ factors are sufficiently constant over the narrow spread of gas temperatures in the hot plasma volume (where these radical species are concentrated) that this level of detail is unwarranted. The corresponding calculated $\{\text{C}_2(\text{a}), \nu = 0\}$ values (2.60×10^{10} , 3.03×10^{12} , and $3.30 \times 10^{13} \text{ cm}^{-2}$) and H($n = 2$) values (2.48×10^8 , 3.18×10^8 , and $2.69 \times 10^8 \text{ cm}^{-2}$) also match well with the CRDS measurements, whereas the calculated $\{\text{OH}(X), \nu = 0\}$ values (5.21×10^{15} , 1.04×10^{14} , and $2.70 \times 10^{13} \text{ cm}^{-2}$) show the correct $X_{\text{C}/\Sigma}$ dependence but seriously overestimate the $\{\text{OH}(X), \nu = 0\}$ values measured in

the oxygen-rich mixture. These variations in radical column densities when moving from an oxygen-rich to a carbon-rich C/H/O plasma (i.e., upon changing $X_{C/\Sigma}$) are clarified by the trends and results presented in Figures 9 and 10 and in Table 2, all of which serve to reinforce the view (from experiment) that the carbon and oxygen based radical species exhibit different spatial distributions and (from the 2-D model) that these species destroy one another by their mutual conversion into CO.

Our previous investigations of MW-activated C/H/(Ar) plasmas^{19,20,23} included power and pressure dependent measurements of $\{\text{CH}(X), \nu = 0\}$, $\{\text{C}_2(\text{a}), \nu = 0\}$, and $\{\text{H}(n = 2)\}$, as revealed by CRDS, and of the corresponding optical emissions. The absorption and emission data were mutually consistent, revealing (under almost all circumstances) monotonic increases in radical density with increasing P and/or p . As shown in Figure 6 (and in the companion OES measurements²⁴), the power and pressure dependences of CH, C_2 , $\text{H}(n = 2)$, and OH in MW-activated C/H/O plasmas are considerably more complex; some species (e.g., OH and C_2) even show opposite trends depending on whether they are monitored by CRDS or by OES. Again, the present 2-D modeling does a very reasonable job in reproducing the observed trends. For example, the 2-D calculations for the base C/H/O mixture with $X_0(\text{H}_2) = 0.3$ predict that $\{\text{CH}(X), \nu = 0\}$, $\{\text{C}_2(\text{a}), \nu = 0\}$, and $\{\text{H}(n = 2)\}$ at $z = 9.5$ mm will increase by, respectively, 16%, 19%, and 19% upon increasing P from 1.0 to 1.5 kW, in good accord with the CRDS measurements (Figure 6a). The calculations also predict that this increase in P should lead to a $\sim 28\%$ increase in $\{\text{OH}(X), \nu = 0\}$, however; whereas, experimentally, it is observed to fall. Similarly, the 2-D modeling of the base $\text{CH}_4/\text{CO}_2/\text{H}_2$ mixture (with $X_0(\text{H}_2) = 0.3$ and $P = 1$ kW) predicts that increasing p from 150 to 200 Torr will result in a 50% increase in $\{\text{C}_2(\text{a}), \nu = 0\}$ at $z = 9.5$ mm but reduce $\{\text{CH}(X), \nu = 0\}$, $\{\text{OH}(X), \nu = 0\}$, and $\{\text{H}(n = 2)\}$ by, respectively, 1%, 16%, and 3% (cf. Figure 6b). A fuller description of these (and the companion OES) data and discussion of the apparent paradoxes they reveal is reserved for the companion article.²⁴

4.5.2. H_2 -Rich C/H/O Plasmas. The 2-D modeling also highlights interesting differences in plasma parameters for the case of an H_2 -rich plasma (i.e., $X_0(\text{H}_2) = 0.95$). Compared with the base $X_0(\text{H}_2) = 0.3$ mixture, the thermal conductivity in the H_2 -rich plasma is ~ 2 -fold higher¹⁸ ($\lambda[\text{W cm}^{-1} \text{K}^{-1}] = 2.3 \times 10^{-5} \times T_{\text{gas}}^{0.76}$), and the maximal gas temperature is consequently lower ($T_{\text{gas}} \approx 2815$ K). That the temperature drop is not larger (recall eq 21) reflects the concomitant reduction in plasma volume (to $V \approx 35$ cm³) and increases in the average power density ($P/V \approx 29$ W cm⁻³) and maximal $n_e \approx 3 \times 10^{11}$ cm⁻³ in the H_2 -rich C/H/O plasma. Such plasma parameter values are much more reminiscent of those found previously for a 4.4% $\text{CH}_4/7\%$ Ar/ H_2 mixture at 1.5 kW,¹⁸ i.e., similar maximal methyl concentrations $[\text{CH}_3] \approx 4 \times 10^{14}$ cm⁻³ are achieved in an annular shell around the hot plasma region, but the radius of this shell is smaller in the case of the H_2 -rich C/H/O plasma, and the maximal $X(\text{H})$ is considerably lower ($X(\text{H}) \approx 5\%$; cf. $X(\text{H}) \approx 9\%$ for a 4.4% $\text{CH}_4/7\%$ Ar/ H_2 mixture¹⁸). The different electron temperatures in the C/H/Ar ($T_e \approx 1.3$ eV) and C/H/O plasmas ($T_e \approx 1.15$ eV for $X_0(\text{H}_2) = 0.95$ and ~ 1.06 eV for $X_0(\text{H}_2) = 0.3$) also merit note. Electron spatial distributions and densities essentially the same as those shown for C/H plasmas in Figure 2 of ref 18 are achieved at lower T_e in H_2 -rich C/H/O plasmas because of the reduced

electron-ion recombination rates: the dominant ion in C/H/O plasmas with $X_0(\text{H}_2) = 0.95$ is H_3O^+ (throughout the range $0.47 \leq X_{C/\Sigma} \leq 0.54$), whereas C_xH_y^+ ions are dominant in a C/H/Ar plasma.

The lower maximal $T_{\text{gas}} \approx 2800$ K values when $X_0(\text{H}_2) = 0.95$ (cf. $X_0(\text{H}_2) = 0.3$) lead to obvious differences in the spatial processing of the input CO_2 and CH_4 , which is more localized around the smaller plasma volume. The predicted volume of CO expansion is clearly smaller and, in contrast to the $X_0(\text{H}_2) = 0.3$ case, the initial $\text{CH}_4/\text{CO}_2/\text{H}_2$ mixture is predicted to expand into all cold regions of the reactor, resulting in conditions where use of a 2-D model to describe what is a 3-D problem (recall section 4.4) becomes more favorable. The closer approach of the input CH_4 and CO_2 , which serve as the source of C_2H_2 and H_2O and the C_xH_y and OH_x radicals in the plasma region, accounts for the seemingly paradoxical finding that the concentrations of C_2H_2 , H_2O , CH_4 , and some C_xH_y and OH_x radicals in the plasma region of a 2.5% $\text{CH}_4/2.5\%$ $\text{CO}_2/95\%$ H_2 mixture are higher than with a 35% $\text{CH}_4/35\%$ $\text{CO}_2/30\%$ H_2 mixture (as can be seen from Table 2), despite the order of magnitude lower C and O input mole fractions in the former. In the H_2 -rich case, the mutual destruction of C_xH_y and OH_x species (i.e., their conversion to CO) is confined to a smaller plasma volume and is more efficiently compensated by diffusion of source species from the peripheral region (i.e., the annular shells of maximal $[\text{C}_2\text{H}_2]$ and $[\text{H}_2\text{O}]$). This explains the gentler $X_{C/\Sigma}$ dependence of the detected radical column densities in the H_2 -rich plasma (recall Figure 4 and Table 2), which, again, is well reproduced by the 2-D model, as are the observed trends in the various column densities: $\{\text{CH}(X), \nu = 0\}$, $\{\text{C}_2(\text{a}), \nu = 0\}$, and $\{\text{OH}(X), \nu = 0\}$ at $z = 9.5$ mm are all predicted to decrease (by factors of 4.9, 23.8, and 1.4) upon increasing $X_0(\text{H}_2)$ from 0.3 (with $X_{C/\Sigma} = 0.5$) to 0.95 ($X_{C/\Sigma} = 0.505$), while $\{\text{H}(n = 2)\}$ is predicted to increase by 9% (cf. Figure 5). Changes in the observed CH^* , C_2^* , C_3^* , CO^* , $\text{H}(n = 3)$, and OH^* emission intensities with $X_{C/\Sigma}$ at base (0.3) and high (0.95) $X_0(\text{H}_2)$, are discussed in the companion paper.²⁴

5. CONCLUSIONS

The chemistry and composition of MW-activated $\text{CH}_4/\text{CO}_2/\text{H}_2$ (and CO/H_2) gas mixtures under conditions relevant to diamond CVD have been investigated by spatially resolved absorption measurements of selected species ($\text{CH}(X)$, $\text{C}_2(\text{a})$, and $\text{OH}(X)$ radicals and $\text{H}(n = 2)$ atoms) localized within the hot plasma region and by companion 2-D modeling. The study provides the first detailed diagnosis and interpretation of the spatially resolved gas processing within such mixtures and shows that, in contrast to the more extensively studied C/H gas mixtures, the plasma composition can depend sensitively on the detail of the C/H/O source gas. Experiment and modeling reveal an obvious switch in the plasma chemistry upon moving from an oxygen rich ($X_{C/\Sigma} < 0.5$) to a carbon-rich ($X_{C/\Sigma} > 0.5$) $\text{CH}_4/\text{CO}_2/\text{H}_2$ gas mixture, thereby providing a rationale for the very limited process window ($X_{C/\Sigma} \approx 0.5-0.54$) for successful diamond growth identified in the Bachmann diagram.

CO and H_2 are the dominant species in the core of these C/H/O plasmas, but within this limited process window, the 2-D modeling reveals many similarities with the more widely used C/H gas mixtures, both with regard to plasma characteristics and the likely diamond growth processes. In both cases, the plasma core is characterized by $T_{\text{gas}} \approx 2800-3000$ K and H atom mole fractions $X(\text{H}) \approx 5-10\%$, around which the gas composition and processing exhibits an annular shell-like

structure which, if $X_{C/\Sigma} > 0.5$, is C_2H_2 rich. This sustains the C_1H_x , C_2H_y , etc., radical densities required for successful diamond growth. CH_3 radicals are identified as the most abundant C_1H_x [$x = 0-3$] species near the growing diamond surface: $[CH_3] \approx 2.5 \times 10^{13}-10^{14} \text{ cm}^{-3}$ for $CH_4/CO_2/H_2$ mixtures with $X_{C/\Sigma} \approx 0.5-0.54$, $X_0(H_2) = 0.3-0.95$, $p = 150$ Torr, and $P = 1 \text{ kW}$, and $[CH_3] \approx 10^{13} \text{ cm}^{-3}$ for the 41.2% $CO/58.8\% H_2$ mixture under base conditions (cf. $[CH_3] \approx 10^{14} \text{ cm}^{-3}$ for a 4.4% $CH_4/7\% Ar/H_2$ mixture, operating at $p = 150$ Torr and $P = 1.5 \text{ kW}$). This, and the similar near-substrate $[H]$ atom densities ($[H] \approx 5 \times 10^{15}-10^{16} \text{ cm}^{-3}$ in the C/H/O plasmas, cf. $\sim 8 \times 10^{15} \text{ cm}^{-3}$ in the base C/H gas mixture), strongly suggests that the same CH_3 radical based diamond growth mechanisms³ prevail in both C/H and C/H/O plasmas. In contrast to MW-activated C/H gas mixtures, however, the present study finds that different gas activation mechanisms prevail in $CH_4/CO_2/H_2$ and CO/H_2 mixtures, thereby revealing a hidden subtlety within the Bachmann diagram.

■ ASSOCIATED CONTENT

📄 Supporting Information

Gas (T_{gas}) and electron (T_e) temperatures, rate coefficients k , and reaction rates $R[\text{cm}^{-3} \text{ s}^{-1}]$ above the substrate center ($r = 0$; $z = 0.5 \text{ mm}$) and in the hot plasma core ($r = 0$; $z = 9.5 \text{ mm}$) returned by the 2-D modeling of a 35% $CH_4/35\%CO_2/30\%H_2$ mixture operating at base conditions ($p = 150$ Torr; $P = 1 \text{ kW}$). This material is available free of charge via the Internet at <http://pubs.acs.org>.

■ AUTHOR INFORMATION

Corresponding Author

*Tel: (117) 9288312. Fax: (117) 9277985. E-mail: mike.ashfold@bris.ac.uk.

Notes

The authors declare no competing financial interest.

■ ACKNOWLEDGMENTS

The Bristol group is grateful to EPSRC for funding (grant no. EP/H043292/1), Element Six Ltd for financial support and the long term loan of the MW reactor, and colleagues K. N. Rosser and Dr. J. A. Smith for their many contributions to the work described here. M.N.R.A. is also grateful to the Royal Society for the award of a Royal Society Leverhulme Trust Senior Research Fellowship.

■ REFERENCES

- Bachmann, P. K.; Leers, D.; Lydtin, H. *Diamond Relat. Mater.* **1991**, *1*, 1.
- Goodwin, D. G.; Butler, J. E. In *Handbook of Industrial Diamonds and Diamond Films*; Prelas, M. A., Popovici, G., Bigelow, L. K., Eds.; Marcel Dekker: New York, 1998; pp 527–581 and references therein.
- Butler, J. E.; Mankelevich, Y. A.; Cheesman, A.; Ma, J.; Ashfold, M. N. R. *J. Phys.: Condens. Matter* **2009**, *21*, 364201 and references therein.
- Kawato, T.; Kondo, K. *Jpn. J. Appl. Phys.* **1987**, *26*, 1429.
- Harris, S. J.; Weiner, A. M. *Appl. Phys. Lett.* **1989**, *55*, 2179.
- Muranaka, Y.; Yamashita, H.; Sato, K.; Miyadera, H. *J. Appl. Phys.* **1990**, *67*, 6247.
- Balestrino, G.; Marinelli, M.; Milani, E.; Paoletti, A.; Pinter, I.; Tebano, A. *Appl. Phys. Lett.* **1993**, *62*, 879.
- Chen, C. F.; Chen, S.; Ko, H.; Hsu, S. E. *Diamond Relat. Mater.* **1994**, *3*, 443.
- Stiegler, J.; Lang, T.; Nygard-Ferguson, M.; von Kaenel, Y.; Blank, E. *Diamond Relat. Mater.* **1996**, *5*, 226.
- Elliott, M. A.; May, P. W.; Petherbridge, J. R.; Leeds, S. M.; Ashfold, M. N. R.; Wang, W. N. *Diamond Relat. Mater.* **2000**, *9*, 311.
- Petherbridge, J. R.; May, P. W.; Pearce, S. R. J.; Rosser, K. N.; Ashfold, M. N. R. *J. Appl. Phys.* **2001**, *89*, 1484.
- Mollart, T. P.; Lewis, K. L. *Diamond Relat. Mater.* **1999**, *8*, 236.
- Gries, T.; de Persis, S.; Vandenbulcke, L.; Met, C.; Delfau, J. L.; de Barros-Bouchet, M. I. *Diamond Relat. Mater.* **2009**, *18*, 730.
- Vandenbulcke, L.; Gries, T.; de Persis, S.; Met, C.; Aubry, O.; Delfau, J. L. *Diamond Relat. Mater.* **2010**, *19*, 1103 and references therein.
- Liang, Q.; Yan, C. S.; Meng, Y. F.; Lai, J.; Krasnicki, S.; Mao, H. K.; Hemley, R. J. *Diamond Relat. Mater.* **2009**, *18*, 698.
- Zhang, Q.; Li, H. D.; Cheng, S. H.; Wang, Q. L.; Li, L. A.; Lv, X. Y.; Zou, G. T. *Diamond Relat. Mater.* **2011**, *20*, 496.
- Issaoui, R.; Achard, J.; Silva, F.; Tallaire, A.; Mille, V.; Gicquel, A. *Phys. Status Solidi* **2011**, *9*, 2023.
- Mankelevich, Y. A.; Ashfold, M. N. R.; Ma, J. *J. Appl. Phys.* **2008**, *104*, 113304.
- Ma, J.; Richley, J. C.; Ashfold, M. N. R.; Mankelevich, Y. A. *J. Appl. Phys.* **2008**, *104*, 103305.
- Ma, J.; Ashfold, M. N. R.; Mankelevich, Y. A. *J. Appl. Phys.* **2009**, *105*, 043302.
- Ma, J.; Richley, J. C.; Davies, D. R. W.; Ashfold, M. N. R.; Mankelevich, Y. A. *J. Phys. Chem. A* **2010**, *114*, 10076.
- Ma, J.; Richley, J. C.; Davies, D. R. W.; Cheesman, A.; Ashfold, M. N. R.; Mankelevich, Y. A. *J. Phys. Chem. A* **2010**, *114*, 2447.
- Richley, J. C.; Fox, O. J. L.; Ashfold, M. N. R.; Mankelevich, Y. A. *J. Appl. Phys.* **2011**, *109*, 063307.
- Richley, J. C.; Kelly, M. W.; Ashfold, M. N. R.; Mankelevich, Y. A. *J. Phys. Chem. A* **2012**, DOI: 10.1021/jp306191y, companion article.
- Western, C. M. *PGOPHER*, A Program for Simulating Rotational Structure; University of Bristol: Bristol, U.K.; see <http://pgopher.chm.bris.ac.uk>.
- Rothman, L. S.; et al. The HITRAN 2008 Molecular Spectroscopic Database. *J. Quant. Spectrosc. Radiat. Transfer*, **2009**, *110*, 533; see <http://www.cfa.harvard.edu/hitran/>.
- Rabeau, J. R.; John, P.; Wilson, J. I. B.; Fan, Y. *J. Appl. Phys.* **2004**, *96*, 6724.
- Wills, J. B.; Smith, J. A.; Boxford, W. E.; Elks, J. M. F.; Ashfold, M. N. R.; Orr-Ewing, A. J. *J. Appl. Phys.* **2002**, *92*, 4213 and references therein.
- Cageao, R. P.; Ha, Y. L.; Jiang, Y.; Morgan, M. F.; Yung, Y. L.; Sander, S. P. *J. Quant. Spectrosc. Radiat. Transfer* **1997**, *57*, 703.
- Luque, J.; Crosley, D. R. *J. Chem. Phys.* **1998**, *109*, 439.
- Rennick, C. J.; Engeln, R. A. H.; Smith, J. A.; Orr-Ewing, A. J.; Ashfold, M. N. R.; Mankelevich, Y. A. *J. Appl. Phys.* **2005**, *97*, 113306.
- Rennick, C. J.; Ma, J.; Ashfold, M. N. R.; Orr-Ewing, A. J.; Mankelevich, Y. A. *Plasma Sources Sci. Technol.* **2006**, *15*, 432.
- NIST Atomic Spectra Database. <http://physics.nist.gov/PhysRefData/ASD/index.html>.
- Rennick, C. J.; Smith, J. A.; Ashfold, M. N. R.; Orr-Ewing, A. J. *Chem. Phys. Lett.* **2004**, *383*, 518.
- Smith, G. P.; Golden, D. M.; Frenklach, M.; Moriarty, N. W.; Eiteneer, B.; Goldenberg, M.; Bowman, C. T.; Hanson, R. K.; Song, C.; Gardiner, W. C., Jr.; Lissianski, V. V.; Qin, Z. *GRI-Mech*; see <http://www.me.berkeley.edu/gri-mech>.
- Richter, H.; Howard, J. B. *Phys. Chem. Chem. Phys.* **2002**, *4*, 2038.
- Wang, H.; Frenklach, M. *Combust. Flame* **1997**, *110*, 173.
- Mankelevich, Y. A.; Orr-Ewing, A. J.; Ashfold, M. N. R. *J. Appl. Phys.* **2007**, *102*, 063310.
- Millar, T. J.; Farquhar, P. R. A.; Willacy, P. K. *Astron. Astrophys. Suppl. Ser.* **1997**, *121*, 139.
- Yoon, J.-S.; Song, M.-Y.; Han, J.-M.; Hwang, S. H.; Chang, W.-S.; Lee, B.; Itikawa, Y. *J. Phys. Chem. Ref. Data* **2008**, *37*, 913.
- Wysong, I. J. *Chem. Phys. Lett.* **2000**, *329*, 42.
- Jensen, M. J.; Bilodeau, R. C.; Safvan, C. P.; Seiersen, K.; Andersen, L. H.; Pedersen, H. B.; Heber, O. *Astrophys. J.* **2000**, *543*, 764.

(43) Aubreton, J.; Elchinger, M.-F.; Hacala, A.; Michon, U. *J. Phys. D: Appl. Phys.* **2009**, *42*, 095206.

(44) Ma, J.; Cheesman, A.; Ashfold, M. N. R.; Hay, K. G.; Wright, S.; Langford, N.; Duxbury, G.; Mankelevich, Y. A. *J. Appl. Phys.* **2009**, *106*, 033305.

(45) Filippov, A. V.; Mankelevich, Y. A.; Pal, A. F.; Rakhimov, A. T.; Serov, A. O.; Suetin, N. V. *Proc. SPIE* **2002**, *4460*, 285.

(46) Cosby, P. C. *J. Chem. Phys.* **1993**, *98*, 7804.

(47) Von Rosenberg, C. W., Jr.; Taylor, R. L.; Teare, J. D. *J. Chem. Phys.* **1971**, *54*, 1974.

(48) Gicquel, A.; Hassouni, K.; Farhat, S.; Breton, Y.; Scott, C. D.; Lefebvre, M.; Pealat, M. *Diamond Relat. Mater.* **1994**, *3*, 581.